

Banner appropriate to article type will appear here in typeset article

The impact of finite span and wing-tip vortices on a turbulent NACA0012 wing

Siavash Toosi^{1,2,3}†, A. Peplinski^{1,2}, P. Schlatter^{3,1,2} and R. Vinuesa^{1,2}‡

¹FLOW, Engineering Mechanics, KTH Royal Institute of Technology, SE-100 44 Stockholm, Sweden

²Swedish e-Science Research Centre (SeRC), Stockholm, Sweden

³Institute of Fluid Mechanics (LSTM), Friedrich-Alexander-Universität (FAU) Erlangen-Nürnberg, 91058 Erlangen, Germany

(Received xx; revised xx; accepted xx)

High-fidelity simulations are conducted to investigate the turbulent boundary layers around a finite-span NACA0012 wing with a rounded wing-tip geometry at a chord-based Reynolds number of $Re_c = 200\,000$ and at various angles of attack up to 10° . The study aims to discern the differences between the boundary layers on the finite-span wing and those on infinite-span wings at equivalent angles of attack. The finite-span boundary layers exhibit: (i) an altered streamwise and a non-zero spanwise pressure gradient as a result of the variable downwash induced by the wing-tip vortices (an inviscid effect typical of finite-span wings); (ii) differences in the flow history at different wall-normal distances, caused by the variable flow angle in the wall-normal direction (due to constant pressure gradients and variable momentum normal to the wall); (iii) laminar flow entrainment into the turbulent boundary layers near the wing tip (due to a laminar/turbulent interface); and (iv) variations in boundary layer thickness across the span, attributed to the variable wall-normal velocity in that direction (a primarily inviscid effect). These physical effects are then used to explain the differences in the Reynolds stress profiles and other boundary layer quantities, including the reduced near-wall peak of the streamwise Reynolds stress and the elevated Reynolds stress levels near the boundary layer edge, both observed in the finite-span wings. Other aspects of the flow, such as the downstream development of wing-tip vortices and their interactions with the surrounding flow, are reserved for future investigations.

Key words:

MSC Codes 76D10, 76F40, 76F65, 76G25.

† Email address for correspondence: siavash.toosi@fau.de

‡ Email address for correspondence: rvinuesa@mech.kth.se

Abstract must not spill onto p.2

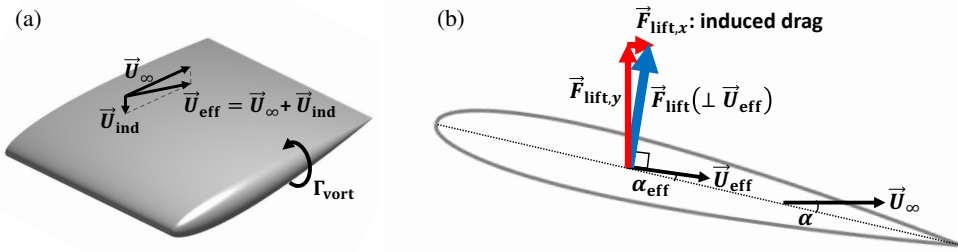


Figure 1: The impact of wing-tip vortices on the effective angle of attack and induced drag: (a) vortex with strength (circulation) Γ_{vort} induces a downward velocity (downwash) of $\vec{U}_{\text{ind}} \approx \Gamma_{\text{vort}}/4\pi d_{\text{vort}}$ (where d_{vort} is the distance along the span to the vortex core) on the wing (cf. Houghton *et al.* 2013); (b) change in the effective angle of attack and generation of a new component of drag, $\vec{F}_{\text{lift},x}$, as a result of deflection of the effective free-stream direction, \vec{U}_{eff} , compared to the geometric free-stream direction, \vec{U}_{∞} .

1. Introduction

A direct result of the pressure difference between the suction and pressure sides of a finite-span wing is the formation of wing-tip vortices and their induced three-dimensionality. Despite the formation of these vortices near the tip, they exert a global influence, affecting the entire span of the wing and giving rise to a complex, three-dimensional (3D) flow.

The most significant impact of the wing-tip vortices on the flow is their induced downwash on the wing, i.e., an induced inviscid velocity normal to the free-stream in the downward direction (cf. Houghton *et al.* 2013). As illustrated in figure 1, this downwash changes the free-stream direction, reducing the effective angle of attack and consequently the lift, while altering the pressure distribution in the process. The change in the pressure distribution (and thus the streamwise pressure gradient) significantly impacts the development of the boundary layers. In addition, as the induced downwash is inversely proportional to the distance from the vortex core (refer to the caption of figure 1), different spanwise locations on the wing encounter varying free-stream directions and a non-uniform pressure distribution along the span. Note that this is a simplified explanation valid for the geometry of figure 1, but the conclusion is generally valid for other wing configurations (cf. Houghton *et al.* 2013). This leads to a spanwise pressure gradient which varies across the chord and span, a non-zero spanwise acceleration, and the formation of boundary layers that exhibit three-dimensional behavior, such as skewed velocity profiles, across a large portion of the wing's span. This non-zero and variable spanwise velocity introduces additional complexities to the boundary layers, which are added to those already present due to adverse or favorable streamwise pressure gradients (cf. Spalart & Watmuff 1993; Perry *et al.* 2002; Aubertine & Eaton 2005; Monty *et al.* 2011; Harun *et al.* 2013; Bobke *et al.* 2017; Bross *et al.* 2019; Pozuelo *et al.* 2022; Devenport & Lowe 2022), as well as spanwise pressure gradients and other three-dimensional effects (cf. Johnston 1960; Perry & Joubert 1965; van den Berg 1975; Rotta 1979; Pierce *et al.* 1983; Bradshaw & Pontikos 1985; Spalart 1989; Moin *et al.* 1990; Degani *et al.* 1993; Johnston & Flack 1996; Ölçmen & Simpson 1995; Coleman *et al.* 2000; Kannepalli & Piomelli 2000; Schlatter & Brandt 2010; Kevin *et al.* 2019; Suardi *et al.* 2020; Devenport & Lowe 2022).

The goal here is to better understand the flow in the vicinity of the wing, and in particular, how the turbulent boundary layers are influenced by the induced three-dimensionality of the finite-span geometry and the resulting wing-tip vortices. This is done by identifying the behaviors present in the finite-span wings which are absent in the limit of infinite span. To do this, a set of high-fidelity simulations is carried out for wings with a symmetric

NACA0012 profile and rounded wing-tip geometry at a chord-based Reynolds number of $Re_c = U_\infty c / \nu = 200\,000$ (where U_∞ is the free-stream velocity, c is the chord, and ν is the kinematic viscosity). Free-flight conditions are considered at angles of attack of $\alpha = 0^\circ$, 5° , and 10° . Additionally, another set of simulations is performed for infinite-span (i.e., periodic) wings with the same profile, Reynolds number, and angle of attack, including an additional configuration of $\alpha = 2^\circ$, which matches the near-root effective angle of attack of the finite-span wing at $\alpha = 5^\circ$. The boundary layers of the finite-span and infinite-span wings are then compared, the discrepancies are identified, and explanations are proposed for the observed differences as well as the underlying mechanisms responsible for them.

The primary focus is on the differences between the finite- and infinite-span wings; thus, common behaviors such as the response to favorable and adverse pressure gradients are excluded from this study. Furthermore, we limit our scope to the regions of the wing which are not dominated by wing-tip vortices or trailing edge effects. For instance, the flow on the suction and pressure sides of the wing possess opposing spanwise components (directed towards the root on the suction side and towards the tip on the pressure side). At the trailing edge, these flows (with different spanwise, streamwise, and wall-normal velocity components) intersect, leading to additional shear and vorticity which could influence both the upstream boundary layers and the downstream wake. Similarly, closer to the tip, especially on the suction side, there are stronger three-dimensional effects and secondary flows present at a more local scale in close vicinity of the wing-tip vortex. The focus here is on regions of the wing that are not dominated by these effects.

Although not directly related to this work, it is worth noting that wing-tip vortices contribute to an additional drag component, known as the induced drag (also called lift-induced drag, or vortex drag; cf. Houghton *et al.* 2013; Federal Aviation Administration 2016). A brief explanation of this is provided in the caption of figure 1. More detailed discussions about this phenomenon, including potential methods to mitigate its effects, can be found in Houghton *et al.* (2013), Federal Aviation Administration (2016), Kroo (2001), Ceron-Munoz *et al.* (2013) and Phillips *et al.* (2019).

Moreover, this work does not present an in-depth study of the structure of wing-tip vortices, their formation, development, and downstream influence. A wealth of research has been dedicated to these topics and is readily available in literature. A few significant studies worth highlighting here include the work of Spalart (1998, 2008), focusing on the development of these vortices in the far wake of an aircraft, and studies by Devenport *et al.* (1996), Chow *et al.* (1997a,b), and Giuni & Green (2013) mainly exploring the near-wake behavior of these vortices in more canonical settings. Other interesting works include studies into the meandering motion of these vortices for rigid and stationary wings (cf. Dghim *et al.* 2021), the impact of the heaving motion of the wing on the structure and development of the wing-tip vortices (cf. Garmann & Visbal 2017; Fishman *et al.* 2017), the interactions of wing-tip vortices with other co-rotating or counter-rotating vortices (Devenport *et al.* 1997, 1999), and the interaction of streamwise-oriented vortices (e.g., wing-tip vortices) upon their incidence on other downstream aerodynamic surfaces (cf. Rockwell 1998; Garmann & Visbal 2015; McKenna *et al.* 2017). We are not aware of any work specifically investigating the influence of the wing-tip vortices on the turbulent boundary layers formed on the wings, which motivated the present study.

The remainder of the paper is structured as follows: Section 2 details the numerical setup, including the solver, computational domain, boundary conditions, grid, and other parameters. The approach for obtaining accurate statistics is also outlined in this section, with more details provided in appendix A. Section 3 describes the general flow field and its most important features, and section 4, which is the main focus of this work, takes a closer look at the impact of finite span and three-dimensionality on the turbulent boundary layers. Finally,

section 5 summarizes the findings, acknowledges the limitations, and discusses potential future directions.

2. Numerical setup

2.1. Numerical solver

The numerical solutions presented in this paper are obtained by solving the incompressible Navier–Stokes equations,

$$\frac{\partial u_i}{\partial t} + u_j \frac{\partial u_i}{\partial x_j} = -\frac{1}{\rho} \frac{\partial p}{\partial x_i} + \nu \frac{\partial^2 u_i}{\partial x_j \partial x_j}, \quad (2.1)$$

under the divergence free constraint, $\partial u_i / \partial x_i = 0$, where u_i and p are the instantaneous velocity and pressure fields, x_i and t are the spatial coordinates and time, and ρ and ν are the fluid density and kinematic viscosity.

These equations are discretized in space and integrated in time using the high-order solver Nek5000, developed by Fischer *et al.* (2010), with adaptive mesh refinement (AMR) capabilities developed at KTH (Peplinski *et al.* 2018; Offermans 2019; Offermans *et al.* 2020; Tanarro *et al.* 2020). Nek5000 is based on the spectral-element method (Patera 1987), essentially a high-order finite-element method, which combines the flexibility of the finite-element formulation in meshing complex geometries with the numerical accuracy of spectral methods (Deville *et al.* 2002). Inside each element, the velocity field is represented by a polynomial of order p (here $p = 7$ in all cases) using Lagrange interpolants on the Gauss–Lobatto–Legendre (GLL) points ($N = p + 1$ GLL points in each direction), while the pressure is represented on $p - 1$ Gauss–Legendre (GL) points following the $P_N - P_{N-2}$ formulation (Maday *et al.* 1987). The nonlinear convective term is overintegrated on a grid with $3N/2$ GL points in each direction, to avoid (or reduce) aliasing errors. Time stepping is performed by an implicit third-order backward-differentiation scheme for the viscous terms and an explicit third-order extrapolation for the nonlinear terms (Karniadakis *et al.* 1991). A high-pass filter relaxation term (Schlatter *et al.* 2004) is added to the right-hand side of the Navier–Stokes equations. This term provides numerical stability and acts as a subgrid-scale (SGS) dissipation. This specific setup has been used and verified in several previous studies (Schlatter *et al.* 2010; Eitel-Amor *et al.* 2014), including wing simulations (Negi *et al.* 2018; Vinuesa *et al.* 2018) and flow around obstacles (Lazpita *et al.* 2022; Atzori *et al.* 2023).

The standard version of Nek5000 is based on hexahedral elements of conforming topology (i.e., no “hanging nodes” are allowed). The AMR version adds the capability of handling non-conforming hexahedral elements with hanging nodes, and so, adds an h -refinement capability where each element can be refined individually. Solution continuity at non-conforming interfaces is ensured by interpolating from the “coarse side” onto the “fine side”. The AMR version includes some modifications to the pressure solver and preconditioner (Peplinski *et al.* 2018), as well as the stiffness matrix and its direct summation operations (Offermans 2019; Offermans *et al.* 2020); however, the majority of the code is identical to the standard version. The AMR version of the code has gone through an extensive verification and validation (V&V) process, including wing simulations (cf. Tanarro *et al.* 2020) and other flows (cf. Offermans *et al.* 2020).

2.2. Computational domain and setup

There are a total of seven different configurations studied in this work. This includes four periodic (infinite-span) wing sections and three finite-span wings. All cases are based on a

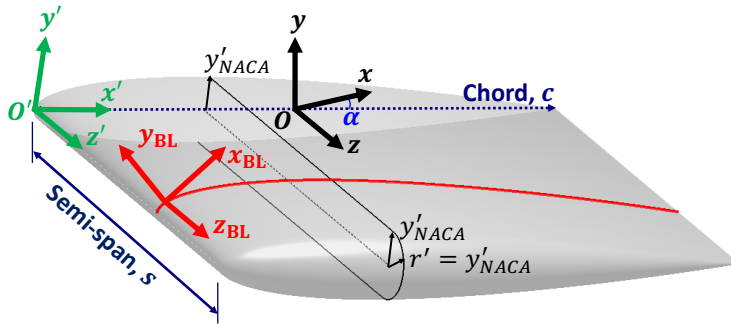


Figure 2: A schematic of the wing-surface definition and its placement in the computational domain with the global Cartesian coordinate system (x, y, z) and its origin O represented in black, the rotated wing coordinate system (x', y', z') and its origin O' represented in green, and the boundary layer coordinate system (x_{BL}, y_{BL}, z_{BL}) represented in red. Note that (x_{BL}, y_{BL}, z_{BL}) is shown at a random location on the wing for visual clarity, while its origin O_{BL} is in fact on O' . The figure also shows the rounded (semi-circle) wing-tip geometry and its definition. The wing has a chord length of c and a semi-span of $s = b/2 = 0.75c$ (dark blue), with a geometric angle of attack of α (blue).

symmetric NACA0012 profile. Both finite- and infinite-span wings have a non-tapered and non-swept planform with zero dihedral angle and no twist. This means that the airfoil chord and angle of attack are constant in the spanwise direction, and the line that connects the leading-edge of the different spanwise sections of the wing is normal to both the free-stream direction and the lift direction (figure 2). The finite-span wings have an aspect ratio (equal to the full-span-to-chord ratio for rectangular planforms) of $b/c = 2s/c = 1.5$ and a rounded wing-tip geometry described by a semi-circle centered at $(y', z')/c = (0, 0.75)$ with a radius equal to the profile thickness at that x' location (see figure 2).

The wings are located such that their mid-chord, $(x', y', z')/c = (0.5, 0, 0)$, coincides with the origin of the global Cartesian coordinate system, $(x, y, z)_O = (0, 0, 0)$, and have a no-slip, no-penetration boundary condition. The computational domain has a rectangular cross-section in the z -normal plane that extends $20c$ upstream, $30c$ downstream, and $20c$ in positive and negative y directions. Different angles of attack are achieved by rotating the wing along the z axis around its center $(x', y')/c = (0.5, 0)$, located at $(x, y) = (0, 0)$, without changing the inflow boundary condition. This specific design is to allow for the use of the “outflow-normal” boundary condition (cf. Deville *et al.* 2002) on y -normal boundaries, which allows for a non-zero y component of velocity (inward at $y = 20c$ and outward at $y = -20c$ in lift-generating configurations). The inflow boundary at $x = -20c$ has a Dirichlet boundary condition with $(u_1, u_2, u_3) = (U_\infty, 0, 0) = \vec{U}_\infty$, while the outlet boundary at $x = 30c$ has the outflow boundary condition. In order to avoid backflow at the outlet there is a sponge region for all $x \geq 10c$ with a gradually increasing forcing term that acts to bring the velocity to its free-stream condition. The effect of the sponge region on the flow has been tested in a number of preliminary runs and deemed negligible for all quantities of interest here.

The finite-span wing domain extends $20c$ in the spanwise direction z from the wing root (located at $z = 0$) and has an “outflow-normal” boundary condition at $z = 20c$. A symmetry boundary condition is used at the $z = 0$ plane (i.e., the wing root). While the symmetry condition forces the z component of the velocity to be zero at the wing root (and thus, for instance, the corresponding Reynolds stress components), the impact of this boundary condition on turbulence quantities appears to be negligible for $z/c \geq 0.05$; therefore,

simulation of full-span wings was not deemed necessary. The infinite-span (periodic) wings share the same domain design and boundary conditions in the xy -plane but have a spanwise width of $L_z = 0.6c$ with periodic boundary conditions in z . The wider L_z in these simulations (compared to previous works, e.g., Hosseini *et al.* 2016; Negi *et al.* 2018; Vinuesa *et al.* 2018) is to allow for a more accurate simulation of the wake region (not discussed here).

The boundary layers are tripped on both the suction and pressure sides in all seven cases. The implemented trip is a randomized time-dependent wall-normal force proposed by Schlatter & Örlü (2012) (also see Hosseini *et al.* 2016) aimed at minimizing the required development length and history effects from the trip. The finite-span wings are only tripped on the main section of the wing ($z < 0.75c$), and not on the wing tip region. On the suction side, the tripping is always located at $x' = 0.1c$ regardless of the angle of attack, while on the pressure side it is at $x' = 0.1c$ for the 0° , 2° and 5° angles of attack and at $x' = 0.25c$ for $\alpha = 10^\circ$. This change in the tripping location on the pressure side of the periodic wing at $\alpha = 10^\circ$ was necessary since the acceleration parameter $K = (\nu/U_e^2) dU_e/dx$ (where U_e is the velocity at the boundary layer edge) far exceeded the rule-of-thumb value of $2.5 - 3 \times 10^{-6}$ for relaminarization (Spalart 1986; Yuan & Piomelli 2015) and the added energy in the tripping region was dissipated before generating turbulence. While this relaminarization was only present in the periodic case, an early decision was made to match the location of the trip for finite- and infinite-span wings at the same geometric angle of attack α . As will be seen in section 4, this was not an optimal choice; however, since it did not have an impact on the quantities studied here and due to the excessive cost of the simulations, this was not modified later.

2.3. Computational grids

The production grids used in this study are generated by iteratively adapting (i.e., refining) an initial grid using the solution-based spectral error indicator introduced by Mavriplis (1990) for turbulent flows. From a mathematical point of view, this error indicator is an approximation of the interpolation error in the numerically-obtained velocity field compared to its estimated exact counterpart (in an L^2 -norm sense), computed by estimating the truncation and quadrature errors (Offermans *et al.* 2020; Tanarro *et al.* 2020). From a physical perspective, this error indicator estimates the sum of the small-scale and unresolved turbulent kinetic energy (Toosi & Larsson 2017), and corresponds to the numerical, modeling (from the LES model), and projection errors (Toosi 2019).

The initial grid for the periodic cases is conformal and originally two-dimensional, which is then extruded (i.e., copied to an appropriate number of spanwise locations) to make sure that the spanwise homogeneity of the mesh is maintained. Different angles of attack share the same near-wing mesh (up to a few boundary layer thicknesses), which is rotated with the wing. The root of the finite-span wing shares a nearly-identical mesh with their periodic counterpart.

The production grids are generated by iterative refinement of the initial grids, where at each iteration elements with the highest contribution to solution error, identified by the volume-weighted error indicator (cf. Lapenta 2003; Park 2003; Toosi & Larsson 2020), are selected for refinement. The convergence process is accelerated by some manual input from the user; for instance, by manually marking the wall elements for refinement. The initial grids are designed to reach their desired wall resolution after four refinements of the near-wall elements. The automatic refinement is continued for a few iterations (where in the first four the wall elements are manually marked for refinement), and the refinement regions are then manually extended for three more iterations (i.e., each element is refined if any of its neighboring elements is refined). This last step helps to avoid repeating the refinement

Case	N_{GLL}	$\Delta t U_\infty / c$	$(\Delta x_{\text{BL}}^+, \delta_1 y_{\text{BL}}^+, \Delta z_{\text{BL}}^+)$	$(\Delta x_{\text{tip}}, \Delta y_{\text{tip}}, \Delta z_{\text{tip}}) / c$	$(\Delta x_{\text{wake}}, \Delta y_{\text{wake}}, \Delta z_{\text{wake}}) / \eta$
P-0	376×10^6	15×10^{-6}	(10.3, 0.72, 8.7)	–	(5.8, 3.6, 3.7)
P-2	383×10^6	18×10^{-6}	(10.3, 0.71, 8.7)	–	(5.8, 3.5, 3.8)
P-5	376×10^6	3.0×10^{-6}	(10.5, 0.73, 8.5)	–	(5.2, 3.2, 3.3)
P-10	438×10^6	7.9×10^{-6}	(12.0, 0.80, 9.0)	–	(6.1, 3.8, 4.0)
RWT-0	952×10^6	16×10^{-6}	(11.4, 0.83, 6.4)	$(11, 1.7, 2.2) \times 10^{-4}$	(5.5, 2.6, 1.7)
RWT-5	1.56×10^9	8.5×10^{-6}	(10.6, 0.77, 5.9)	$(11, 1.7, 2.2) \times 10^{-4}$	(5.6, 2.8, 1.8)
RWT-10	2.16×10^9	6.3×10^{-6}	(9.9, 0.72, 5.5)	$(11, 1.7, 2.2) \times 10^{-4}$	(5.6, 3.0, 1.9)

Table 1: Description of the production grids used in this study. The naming convention distinguishes the different setups by P- α for periodic wings at an angle of attack of α and RWT- α for finite-span wings at α° angle of attack. N_{GLL} is the total number of GLL points (the number of independent grid points is around $0.67N_{\text{GLL}}$). All Δ 's are based on the mean resolution computed as the element size divided by the polynomial order, whereas $\delta_1 y_{\text{BL}}$ is the distance from the wall of the first GLL point off the wall. Wall resolutions, including both Δ^*_{BL} and Δ^*_{tip} , are reported along the wall coordinates $(x_{\text{BL}}, y_{\text{BL}}, z_{\text{BL}})$ (figure 2). The boundary layer resolutions Δ^*_{BL} are normalized by the viscous length δ_ν and reported at $(x', z')/c = (0.7, 0.3)$ for the element on the wall. Tip resolutions Δ^*_{tip} are normalized by the chord c and reported at $x'/c = 0.7$ and $z' = z'_{\text{max}}$. Wake resolutions Δ^*_{wake} are reported at $(x, z)/c = (2, 0.3)$ at the location of minimum mean velocity.

process further (a process which becomes expensive for these progressively finer grids) and leads to a smoother and more uniform mesh. The adaptation process is terminated after reaching the resolution criteria from literature (such as those used in Vinuesa *et al.* 2017b, 2018), expressed in terms of the viscous length scale, $\delta_\nu = \nu \sqrt{\rho/\tau_w}$ (where τ_w is the wall shear stress) for the boundary layer mesh, and the Kolmogorov length scale $\eta = (\nu^3/\epsilon)^{1/4}$ (where ϵ is the local isotropic dissipation rate) for the wake region (cf. Pope 2000).

Table 1 summarizes some of the characteristics of the production grids used in this work. Note that the finite-span wings require significantly larger numbers of grid points compared to the periodic cases. This is partly to resolve the tip region and the larger span of these wings, and partly because of the decision to perform these simulations at slightly higher resolutions due to the potential insufficiency of the resolution criteria originally verified for canonical flows. For similar reasons, wings at higher angles of attack require higher numbers of grid points to accurately resolve all the important features of their more complex flow field with stronger vortices and secondary flows.

Figure 3 shows the spectral elements of the RWT-10 grid, as a representative example of the grids used in this study, with instantaneous vortical structures of the flow visualized using the λ_2 vortex identification method (Jeong & Hussain 1995) added for visual reference.

2.4. Flow transients and statistical averaging

Flow transients are removed both during the grid-adaptation stage and after reaching the production grid. In total, a minimum of approximately $80c/U_\infty$ (equivalent to 80 convective time units, $\mathcal{T}_{\text{conv}} = c/U_\infty$) of integration time is discarded as transients. This comprises $50\mathcal{T}_{\text{conv}}$ on the coarse initial grid, roughly $25\mathcal{T}_{\text{conv}}$ on various adapted grids before reaching the production grid, and an additional $4\mathcal{T}_{\text{conv}}$ on the production grid.

After the transient period, turbulence statistics are collected over a period of $5\mathcal{T}_{\text{conv}}$ or above in the periodic cases (P-0, P-2, P-5, P-10), around $8\mathcal{T}_{\text{conv}}$ for RWT-0, around $14\mathcal{T}_{\text{conv}}$ for RWT-10, and for a longer period of around $23\mathcal{T}_{\text{conv}}$ in RWT-5. Table 2 summarizes the

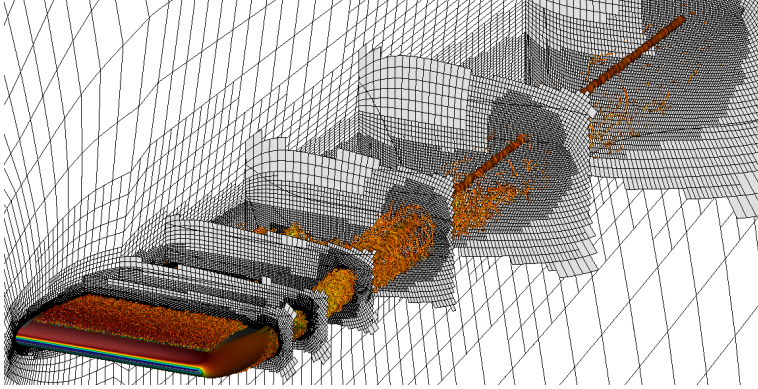


Figure 3: An example of the grids used in this study. Edges of the spectral elements of RWT-10 (with 4.23 million spectral elements; see table 1) are shown by black lines on a number of planar slices. The grid is generated using the h -adaptation capabilities of the AMR version of Nek5000. The figure also shows instantaneous vortical structures represented by isosurfaces of $\lambda_2 c^2 / U_\infty^2 = -100$ colored by streamwise velocity ranging from low (blue) to high (red) for visual reference.

Case	$t_{\text{avg}}/\mathcal{T}_{\text{conv}}$	$\mathcal{T}_{\text{conv}}/\mathcal{T}_{\text{ETT,ss}}$	$\mathcal{T}_{\text{conv}}/\mathcal{T}_{\text{ETT,ps}}$	$\mathcal{T}_{\text{conv}}/\mathcal{T}_{\text{shear}}$	$\mathcal{T}_{\text{conv}}/\mathcal{T}_{\text{vort}}$
P-0	6.1	2.4	2.4	16.4	–
P-2	4.9	2.1	2.7	16.4	–
P-5	5.8	1.6	2.9	13.0	–
P-10	5.7	0.54	3.7	9.0	–
RWT-0	8.2	2.5	2.5	14.0	–
RWT-5	23.2	1.9	3.0	14.3	2.3
RWT-10	14.1	1.4	3.2	14.3	2.6

Table 2: A summary of the averaging time t_{avg} used in each case compared to different time scales in the flow. $\mathcal{T}_{\text{conv}}$ is the convective (flow-over) time scale, \mathcal{T}_{ETT} is the boundary layer eddy turnover time reported at $(x', z')/c = (0.7, 0.3)$, $\mathcal{T}_{\text{shear}}$ is the shear time scale in the wake reported at $(x, z)/c = (2.0, 0.3)$, and $\mathcal{T}_{\text{vort}}$ is the time scale of vortex rotation reported at $x/c = 2.0$. Subscripts \cdot_{ss} and \cdot_{ps} stand for the suction side and pressure side of the wing. Definition of time scales is given in the text.

averaging time t_{avg} used in each simulation in terms of the convective time unit. A conversion ratio is provided to relate $\mathcal{T}_{\text{conv}}$ to other time scales of the flow, including: the boundary layer eddy-turnover time $\mathcal{T}_{\text{ETT}} = \delta_{99}/u_\tau$, where δ_{99} is the 99% boundary layer thickness and $u_\tau = \sqrt{\tau_w/\rho}$ is the friction velocity; the shear-layer (wake) time scale $\mathcal{T}_{\text{shear}} = \delta_{0.5,\text{shear}}/U_\infty$, where $\delta_{0.5,\text{shear}}$ is a measure of the wake thickness (see Pope 2000); the vortex-rotation time scale $\mathcal{T}_{\text{vort}} = \pi d_{\text{vort}}/u_{\theta,\text{max}}$, where $u_{\theta,\text{max}}$ is the maximum azimuthal velocity around the vortex core and d_{vort} is the vortex diameter measured as the distance between the two peaks in the azimuthal velocity around the core. The RWT-0 (which is symmetric around the $y = 0$ plane and can be averaged in that direction) and RWT-5 have similar effective values of $t_{\text{avg}}/\mathcal{T}_{\text{ETT,ss}}$ (which is the most relevant time scale for the quantities studied here), while RWT-10 has a shorter integration time due to computational-cost constraints.

The statistics are collected on the fly (see appendix A for more details) at a sampling rate that is around an order of magnitude higher than the highest frequency of the flow, here dictated by the viscous time scale $\nu/u_\tau^2 (\geq 2 \times 10^{-3} \mathcal{T}_{\text{conv}}$ for cases studied here). The

periodic cases are homogeneous in the spanwise direction and therefore an ensemble average in that direction is also performed when computing the statistics. While RWT-0, RWT-5, and RWT-10 are fully three-dimensional flows and exhibit a variation of solution statistics along the span, these variations are smooth over the turbulent boundary layer section of the wings. This allows for a spanwise filtering of the statistics using a (wide) Gaussian filter with a variable filter width that is adjusted based on flow physics and resembles an averaging process. This procedure is explained in more detail in appendix A.

The temporally and spatially averaged (or filtered) fields are denoted by $\langle \cdot \rangle$; e.g., $\langle u_i \rangle$ and $\langle p \rangle$ for the mean velocity and mean pressure fields. The fluctuating part is then defined as the (pointwise) difference between the instantaneous and mean values; e.g., $u'_i = u_i - \langle u_i \rangle$ and $p' = p - \langle p \rangle$ for the fluctuating velocity and pressure fields.

In each case, the full statistical record is divided into four or more batches of equal size, which are used to estimate the uncertainty in solution statistics by computing the confidence intervals of each quantity of interest using the non-overlapping batch method (cf. Conway 1963). Given the higher sensitivity of the Reynolds stresses, particularly for finite-span wings, their approximate error bars are included in the comparisons in section 4.3 and appendix C. With the use of ensemble averaging along the span in periodic cases and the equivalent filtering in the wing-tip cases, the averaging times used in this work are deemed sufficient for the discussions here.

3. Flow around the finite-span wings

This section describes the important features of the flow around the finite-span wings of this study relevant to the discussions in section 4 and, to a certain degree, serves as an introduction to that section.

3.1. The instantaneous flow field

The flow around RWT-0, RWT-5 and RWT-10 is illustrated in figure 4 by the instantaneous vortical structures of the flow using the λ_2 visualization method of Jeong & Hussain (1995). The figure visualizes the turbulent boundary layers formed on the wings, the turbulent wake, and the wing-tip vortex identified as a cylindrical structure (surrounded by turbulent structures) that separates from the wing somewhere close to the tip and remains coherent for a long distance downstream of the wing (the entire field of view in figure 4). Note that the wing-tip vortex is only present in lift-generating configurations and absent in RWT-0. As expected, RWT-10 has a stronger wing-tip vortex (leading to a larger vortex diameter for a fixed value of λ_2) which impacts a larger portion of the wing, and more strongly, compared to RWT-5. While not directly relevant to the discussions of section 4, it is interesting to note that the vortex core in RWT-10 has a higher streamwise velocity compared to RWT-5, which is associated in the literature to the lower core pressure of the stronger wing-tip vortex and thus flow entrainment into the core region (cf. Lee & Pereira 2010).

The location of tripping and its effectiveness is visually clear in figure 4 by the absence of turbulent structures upstream of the trip and the presence of hairpin vortices (which the trip introduces through wall-normal forcing) downstream of the tripping line. The relatively low friction Reynolds number of the flow ($200 \lesssim Re_\tau \lesssim 300$, see tables 3, 4, and 5 in appendix C) is apparent from the hairpin-dominated structure of the turbulent boundary layers (cf. Eitel-Amor *et al.* 2015). Note that on both the suction and pressure sides the tripping line extends throughout the span of the wing from the root to the tip, but does not include the wing tip region (the semi-circle shown in figure 2). This results in a laminar flow around the wing tip and a laminar/turbulent interface at the spanwise end of the tripping line.

The figure shows a strong flow convection from the pressure side to the suction side

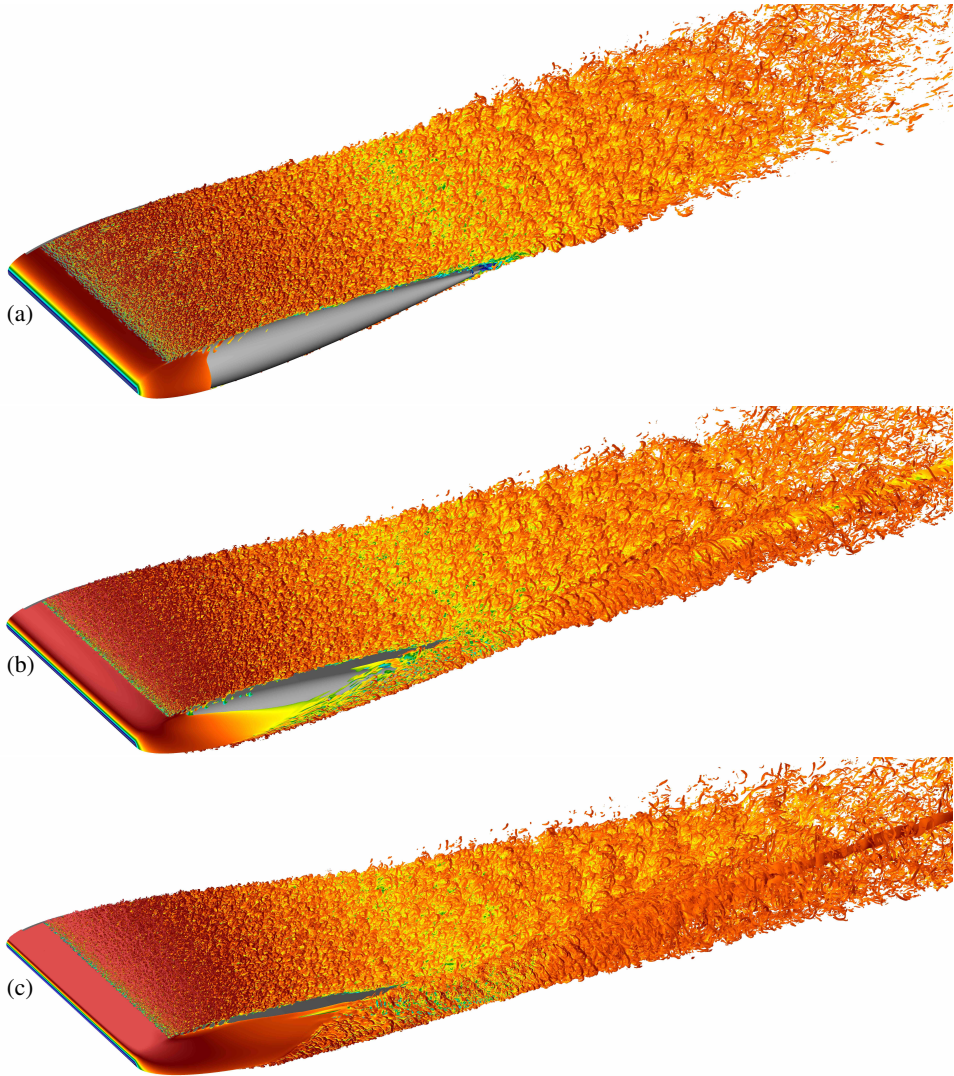


Figure 4: An overview of the flow around the finite-span wings: (a) RWT-0, (b) RWT-5, and (c) RWT-10. Plots show the instantaneous vortical structures, visualized by iso-surfaces of $\lambda_2 c^2 / U_\infty^2 = -100$ colored by u_1 / U_∞ from -0.3 (blue) to 1.3 (red). The wing surface is shown in light grey.

(visualized by the convected turbulent structures from the pressure side), starting from the leading edge of the wing. This underscores the global impact of the finite span of the wing and the wing-tip vortices on the entire flow field. RWT-10 generates a higher lift and thus has stronger pressure gradients, leading to a stronger flow convection, stronger wing-tip vortices, and stronger three-dimensionality in the flow field.

It is also important to note the appearance of a non-turbulent area on the suction side of RWT-5 and RWT-10 in a region close to the wing-tip vortex. This might initially suggest a relaminarization of the turbulent boundary layer due to the increased pressure gradient, rotation and flow acceleration in the vicinity of the wing-tip vortex. However, upon further investigation this was proved not to be the case, since the turbulent region of the boundary layer was almost exactly following the streamlines of the flow released at the edge of the

boundary layer near the spanwise end of the tripping line. In other words, the appearance of this laminar region should be primarily attributed to the non-zero spanwise velocity towards the root that convects the spanwise laminar/turbulent interface of the boundary layer in that direction and causes a laminar region to appear near the wing tip region. Nevertheless, the present behavior does not mean that extending the tripping line to include the tip region will necessarily lead to a fully turbulent suction side, since the strong flow acceleration, rotation and pressure gradients might still be sufficiently high to result in relaminarization.

3.2. Mean-flow streamlines

The extent of three-dimensionality of the flow and its impact on the boundary layers are shown in figure 5 using the streamlines obtained from the mean velocity field $\langle u_i \rangle$. The large deflection angle of the streamlines can be easily observed by comparison to the approaching free-stream direction (chord-wise lines). As expected, this deflection increases for all cases closer to the tip. Note that the deflection from the free-stream direction starts at the beginning of the boundary layer development and spans across a large region of the wing (almost the entire semi-span for these low aspect ratio wings). An interesting observation is that the streamlines of RWT-0 (which does not have a wing-tip vortex) are still impacted by the finite-span of the wing and deflected towards the root, albeit with a lower deflection angle compared to RWT-5 and RWT-10. This is the reason for the appearance of a small laminar region close to the trailing edge of RWT-0 in figure 4 (a). The other interesting observation is the large spanwise extent of the impacted boundary layer streamlines on the pressure side of RWT-5 and RWT-10 which is comparable to their suction side. On both the suction and pressure sides, the deflection angle approaches zero at the root of the wing as a result of the symmetry.

The more interesting observation from figure 5 is that the deflection angle of streamlines varies in the wall-normal direction across the boundary layer thickness δ_{99} . The streamlines closer to the wall have a larger deflection angle compared to those farther from the wall, and this is true on both the suction and pressure sides and at all spanwise locations. This is a common feature observed in many three-dimensional boundary layers (cf. Johnston 1960; Perry & Joubert 1965; Pierce *et al.* 1983; Ölçmen & Simpson 1995; Devenport & Lowe 2022) which happens due to the lateral pressure gradient encountered by the boundary layer and the variable balance between the different terms of the momentum equation, such that the fluid closer to the wall (which has a lower momentum) responds faster to the pressure gradient (cf. Devenport & Lowe 2022, and references therein). The variable deflection angle of the streamlines in the streamwise, wall-normal, and spanwise directions has a number of consequences on the boundary layers which will be discussed further in section 4.

The wing-tip vortices are visible in RWT-5 and RWT-10 in figures 5 (b) and (c) as streamlines that are clustered together and formed into spirals on the suction side of the wings. Additional details about the flow in the vicinity of the tip can be found in appendix B. The generated wing-tip vortex impacts the surrounding flow differently depending on the distance. This is primarily related to the velocity induced by the vortex (the Biot-Savart law), which is proportional to the inverse of the distance from the vortex core (refer to the caption of figure 1) and approximately in the azimuthal direction of a cylindrical coordinate system with the vortex core at its origin. Due to the large variations in both magnitude and direction of the induced velocity, the flow in the vicinity of the vortex core is highly non-homogeneous. The flow acceleration due to pressure gradient is also larger near the tip. At larger spanwise distances from the vortex—and farther downstream from the location of its initial formation—the induced velocity on the wing surface becomes a nearly uni-directional downwash with a variable magnitude (and thus, a variable effective angle of attack along the

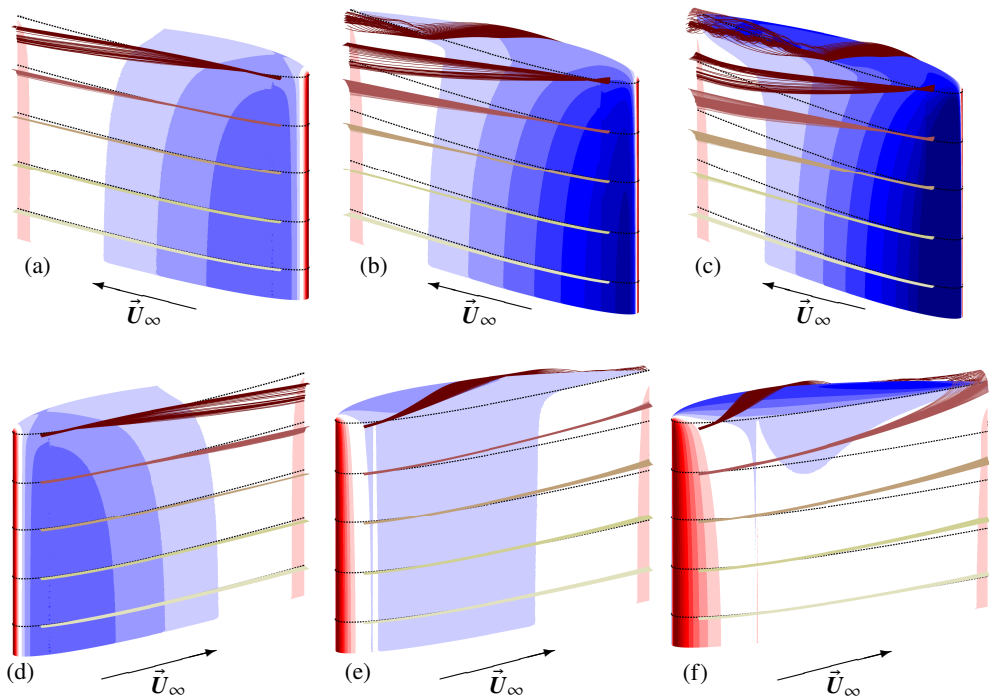


Figure 5: Contour plots of the pressure coefficient c_p on the wing surface for (a, d) RWT-0, (b, e) RWT-5 and (c, f) RWT-10 on the suction side (a, b, c) and pressure side (d, e, f) of the wings. Contour plots are overlaid with streamlines released at $x'/c = 0.12$ at different z'/c locations (0.1, 0.26, 0.43, 0.59, 0.75). The contour levels are from -1 (dark blue) to 1 (dark red) in increments of 0.1. The dotted black lines on the wing surface show the chord-wise direction (i.e., constant z' , equivalent to the approaching free-stream direction) at the same spanwise locations as the streamlines are released as a visual reference for their deflection. Arrows indicate the approximate direction of the free-stream velocity U_∞ .

span). We will take advantage of this behavior of finite-span wings to facilitate the analyses in section 4.

Figure 5 also shows the contour lines of the pressure coefficient $c_p = 2(p - p_\infty)/\rho U_\infty^2$ on the surface of the wings. Note that the wall-parallel component of pressure-gradient (at the wall and across the boundary layer thickness) is orthogonal to the constant c_p lines represented in the figure. An increasing trend in the pressure coefficient (and therefore pressure) can be observed approaching the tip region. This pressure gradient is the main cause for the observed streamline deflections in RWT-0. The boundary layer streamlines on the suction side of RWT-5 and RWT-10 are deflected towards the root as a result of these pressure gradients and the high momentum of the flow approaching the suction side from the pressure side. There is also a pressure gradient on the pressure sides of RWT-5 and RWT-10, albeit weaker, which causes the flow to accelerate towards the tip of the wing. On both sides, the pressure gradient decreases in magnitude and becomes more aligned with the streamlines closer to the wing root (characterized by contour level lines that are more aligned with the spanwise direction and farther apart from each other). This implies that the fluid particles following the streamlines are subjected to reduced accelerations due to pressure gradient. Consequently, the streamlines approximate straighter lines, leading to less variation in the

deflection along a given streamline. This in turn mitigates some of the three-dimensional effects that result from the skewed velocity profile.

4. Turbulent boundary layers

The finite span of the wings and the induced three-dimensionality by the wing-tip vortices have a number of important impacts on the boundary layers developing on RWT-0, RWT-5, and RWT-10. The goal of this section is to separate and simplify these effects as much as possible in sections 4.1 and 4.2, before analyzing the remaining finite-span effects more closely in section 4.3.

4.1. The impact of the effective angle of attack

Figure 6 plots the 99% boundary layer thickness δ_{99} defined based on the diagnostic scaling (Vinuesa *et al.* 2016) and the Clauser pressure-gradient parameter $\beta_{x_{BL}}$ (Clauser 1954, 1956), at a spanwise location near the root. The Clauser parameter is computed along x_{BL} (defined in figure 2) as,

$$\beta_{x_{BL}} = \frac{\delta^*}{|\tau_w|} \frac{\partial P_e}{\partial x_{BL}}, \quad (4.1)$$

where δ^* is the boundary layer displacement thickness, $|\tau_w|$ is the shear-stress magnitude at the wall, and $P_e = \langle p(x_{BL}, \delta_{99}, z_{BL}) \rangle$ is the pressure at the edge of the boundary layer.

There is a large difference between the boundary layers formed on the finite-span wings compared to the periodic ones at the same angle of attack. Namely, the boundary layers on the suction sides are thinner and encounter lower adverse pressure gradients (lower $\beta_{x_{BL}}$ values), while they are thicker on the pressure side and encounter a larger Clauser parameter (interesting to note that $\beta_{x_{BL}} > 0$ over the majority of the pressure side as well). Furthermore, the discrepancies are larger for higher angles of attack and nearly vanish for $\alpha = 0^\circ$. These are all consequences of the lower effective angle of attack α_{eff} of the finite-span wings compared to their geometric angle of attack α (a well-known inviscid effect caused by the induced downwash of the wing-tip vortex, explained in figure 1). This is further demonstrated by figure 7 which shows the section-wise pressure component of the lift and drag coefficients of all cases defined as,

$$c_{L,p}(z_0) = \frac{2}{\rho U_\infty^2 c} \oint (\langle p(x_{BL}, 0, z_0) \rangle \cdot \mathbf{e}_n) dx_{BL},$$

$$c_{D,p}(z_0) = \frac{2}{\rho U_\infty^2 c} \oint (\langle p(x_{BL}, 0, z_0) \rangle \cdot \mathbf{e}_t) dx_{BL},$$

where \mathbf{e}_n is a unit vector normal to the wall and opposite to y_{BL} , \mathbf{e}_t is a unit vector tangential to the wall in the same direction as x_{BL} , and ρ and c are the fluid density and chord length. The integrals are taken on the wing surface ($y_{BL} = 0$) over both the suction and pressure sides at a fixed spanwise location $z_{BL} = z_0$. Assuming a linear variation of the lift coefficient with angle of attack in infinite-span wings (which is approximately true for relatively low angles of attack; cf. Houghton *et al.* 2013; Federal Aviation Administration 2016) we could make the approximation that $3^\circ \leq \alpha_{\text{eff}} \leq 4.5^\circ$ for RWT-10 (with it being closer to 4.5° at the root and around 3° close to the tip) and $1^\circ \leq \alpha_{\text{eff}} \leq 2^\circ$ for RWT-5 (the lifting-line theory (cf. Houghton *et al.* 2013) leads to similar approximated values for α_{eff} over the majority of the span). This justifies the fact that in figure 6 both the boundary layer thickness and the Clauser parameter on the suction side of RWT-10 are very close to those of the P-5, or why the RWT-5 curves (corresponding to $\alpha_{\text{eff}} \approx 2^\circ$ at the root) are closer to P-2.

It is important to emphasize that the observed similarity based on effective angles of attack

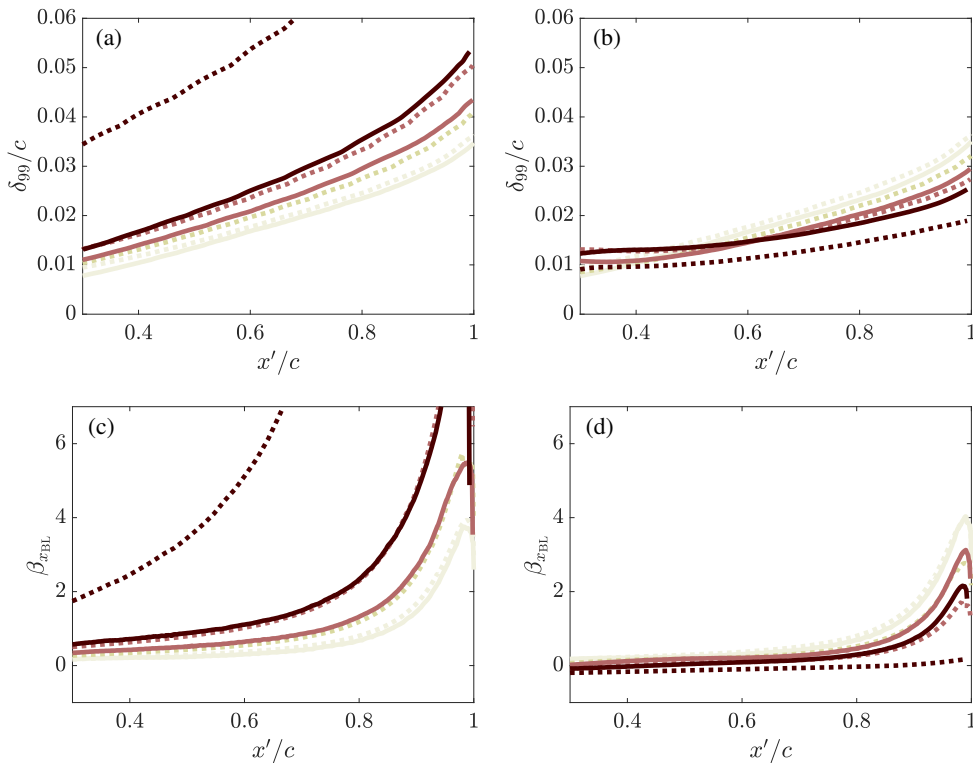


Figure 6: The 99% boundary layer thickness δ_{99} (a, b) and the Clauser pressure-gradient parameter β_{xBL} (c, d) plotted at $z'/c = 0.1$ (close to the root) on the suction side (a, c) and pressure side (b, d) of the wings of this study. The finite-span wings are plotted in solid lines, while periodic airfoils are shown by the dotted lines. Colors, from light to dark, correspond to angles of attack of $\alpha = 0^\circ, 2^\circ, 5^\circ,$ and 10° , respectively, for infinite-span wings. The three finite-span wings are shown with matched colors to the infinite-span ones at the same α . The observed differences are mainly attributed to the impact of the reduced effective angle of attack α_{eff} (an inviscid effect caused by the induced downwash of the wing-tip vortex; see figure 1) on the boundary layers.

is in fact a result of an approximate similarity of the pressure gradient and boundary layer histories. Therefore, our reliance on α_{eff} in the next sections is meant as an approximate equivalence of pressure gradients and history effects. In fact, there are additional (inviscid) effects caused by a positive (i.e., away from the wall) and variable wall-normal velocity along the span, especially near the tip at locations earlier in the development of the wing-tip vortex, that are not captured by the simplified use of α_{eff} . These effects will be discussed further in section 4.3.

Figure 7 (a) also compares the turbulent finite-span wings, RWT-0, RWT-5, and RWT-10, with inviscid (incompressible Euler) simulations of the same setups (without the tripping) performed using the open-source solver SU2 (Economou *et al.* 2016). The nearly identical variation of the lift (and effective angle of attack) over a large portion of the span emphasizes the inviscid nature of the phenomenon. The larger observed differences near the tip should be mainly attributed to the difference in vortex formation and the resulting change in both the vertical and spanwise location of the vortex in inviscid flows. These differences are discussed briefly in appendix B. Additional viscous effects are present near the tip and are expected

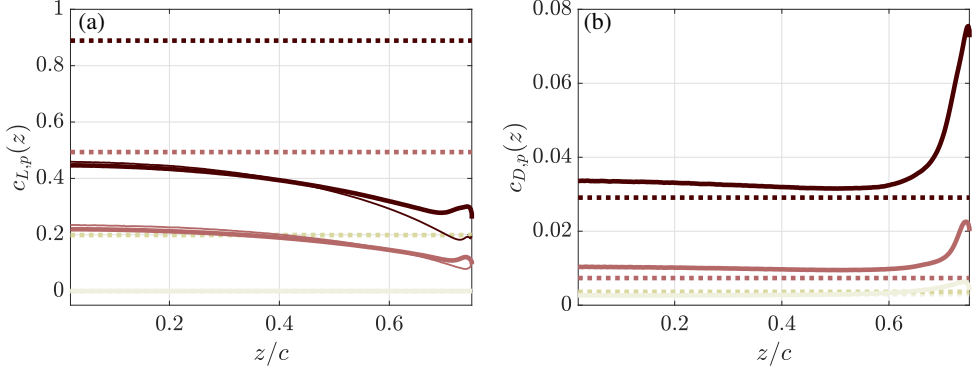


Figure 7: The section-wise (a) pressure lift and (b) pressure drag coefficients along the span for all the geometries of this study. Line styles and colors are the same as those in figure 6. The additional thin solid lines in panel (a) are from inviscid simulations of finite-span wings for the same configurations as RWT-0, RWT-5, and RWT-10. The nearly identical variation of pressure lift coefficient (approximately proportional to α_{eff}) emphasizes the inviscid nature of the phenomenon. Refer to figure 1 (b) and its caption for a schematic explanation of the induced drag which explains the increased drag coefficient of the finite-span wings.

to contribute to the observed differences in that region; however, they will not be discussed here.

4.2. Collateral flow and transformation into wall-shear coordinates

The skewed velocity profile and the variable deflection angle of the streamlines (figure 5) result in additional non-zero velocity gradient components, and consequently, the activation of additional production terms in the transport equations of \tilde{R}_{13} , \tilde{R}_{23} , and \tilde{R}_{33} (for $\tilde{R}_{ij} = \langle u'_i u'_j \rangle_{\text{BL}}$ denoting the Reynolds stress expressed in $(x_{\text{BL}}, y_{\text{BL}}, z_{\text{BL}})$ coordinates) with the largest impact on the production of \tilde{R}_{13} .

The main goal of this section is to use the flow characteristics to find a coordinate system that simplifies the analysis.

Figure 8 plots the deflection angle γ_{stream} defined as the angle between the wall-parallel part of the velocity vector and the wall-parallel direction x_{BL} (with the wall-normal component of the velocity vector $\langle u_2 \rangle_{\text{BL}}$ excluded). Visually, this is the angle that the streamlines of figure 5 make with the chord-wise lines (free-stream direction). While γ_{stream} is highly variable across the boundary layer thickness, it exhibits an important quality: it is approximately constant in the most active and important region of wall turbulence, $y_{\text{BL}}^+ \leq 30$. This region of *collateral flow* is a common feature of many three-dimensional boundary layers (cf. Johnston 1960; Perry & Joubert 1965; Pierce *et al.* 1983; Ölçmen & Simpson 1995; Devenport & Lowe 2022). In the context of our discussion, this means that the most active part of the near-wall region can potentially be considered nearly two-dimensional in a rotated coordinate system that is aligned with the direction of the streamlines in the $y_{\text{BL}}^+ \leq 30$ region. The region above 30δ , still experiences a variable shear, but since both the Reynolds stresses and mean velocity gradients are significantly smaller in this region, the contribution from the new production terms (which are the product of the Reynolds stresses and the mean velocity gradient) will remain low for a large portion of the boundary layer.

In the rest of this paper the boundary layers are studied in a coordinate system (x_τ, y_τ, z_τ) , which is defined by rotating $(x_{\text{BL}}, y_{\text{BL}}, z_{\text{BL}})$ (figure 2) around its wall-normal axis y_{BL} in such a way that x_τ becomes aligned with the direction of the wall shear stress (the streamlines).

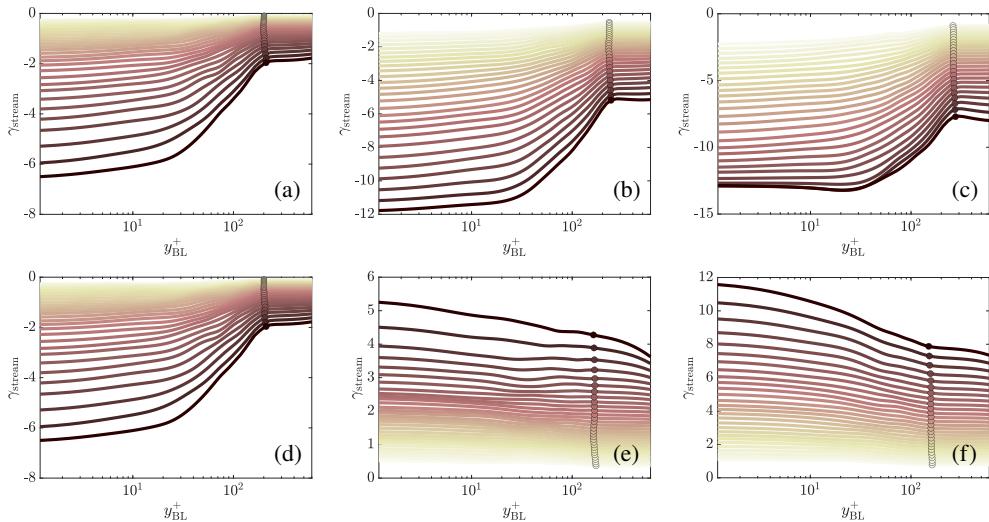


Figure 8: The deflection angle (in degrees) at $x'/c = 0.7$ for multiple spanwise locations from $z'/c = 0.1$ to 0.6 (with 0.02 increments) on the suction side (a, b, c) and the pressure sides (d, e, f) of (a, d) RWT-0, (b, e) RWT-5, and (c, f) RWT-10. Darker colors are sampled closer to the tip. Circles show the edge of the boundary layer, δ_{99} . Negative (positive) γ_{stream} values correspond to deflection towards the root (tip). Note the relatively constant value of γ_{stream} for $y_{\text{BL}}^+ \leq 30$.

Note that the orientation of this coordinate system changes across both the span and the chord of the wing (see the streamlines of figure 5). This does not affect the analysis in the rest of the paper which is performed in local coordinates.

The rotated Reynolds-stress components exhibit a structure that is very close to a two-dimensional boundary layer, where $R_{13} \approx R_{23} \approx 0$ (for $R_{ij} = \langle u'_i u'_j \rangle_\tau$ denoting the Reynolds stress expressed in (x_τ, y_τ, z_τ) coordinates). This simplification is possible for these boundary layers mostly because of the relatively small change in the deflection angle across the boundary layer thickness (less than 10° ; see figure 8) and is not necessarily possible for all three-dimensional boundary layers. The spanwise component of the mean velocity is by definition close to zero for $y_\tau^+ \leq 30$ in this coordinate system and only increases closer to the edge of the boundary layer. This results in a Reynolds-stress production term close to that of a statistically two-dimensional boundary layer for similar conditions. The obtained simplification by rotation into the (x_τ, y_τ, z_τ) coordinate system cannot remove the less local effects. Such effects are discussed in the next section.

4.3. Additional departures from infinite-span wings

Two other notable effects are associated with the finite span of the wing and the three-dimensional flow field:

(i) Flow acceleration from the pressure side towards the suction side, during the formation of the wing-tip vortices, results in a wall-normal velocity that is different along the chord and the span of the wing. This variation is such that the locations closer to the tip and earlier in the development of the wing-tip vortex (i.e., closer to the leading edge) experience higher positive wall-normal velocities. The wall-normal velocity impacts the development of the boundary layers, such that increased values of this quantity lead to a faster growth rate. As a result, there is a slight increase in δ_{99} on the suction side for locations closer to the tip, and

similarly thinner boundary layers closer to the tip on the pressure side. This is primarily an inviscid effect.

(ii) Variation of the deflection angle with normal distance from the wall (a result of variable momentum across y_τ , mainly due to viscous effects) means that streamlines crossing a wall-normal line have converged from different spanwise locations on the wing. Since the effective angle of attack, and thus the streamwise pressure gradients, are different at different spanwise locations (mostly an inviscid effect), fluid particles at different wall-normal locations have experienced different histories. This effect is larger closer to the tip region, where both the variation in the deflection angle (see figure 8) and the variation in the pressure gradient (approximately characterized by the effective angle of attack; see figure 7) are larger.

This section investigates and characterizes these effects by comparing the boundary layers formed on the finite-span wings with their equivalent from the infinite-span wings. Equivalence is quantified here as closeness in terms of the local values of Re_τ and β_{x_τ} , as well as similarity of their history. Appendix C explains in more detail the procedure used to match each of these quantities. The importance of this procedure is discussed briefly at the end of this section.

Figure 9 depicts the variation of the normal streamwise Reynolds stress, $R_{11} = \langle u'_1 u'_1 \rangle_\tau$, in RWT-5 as a function of the streamwise and spanwise locations. Additional Reynolds stress components, additional locations, and other angles of attack are included in figures 12, 13, and 14 in appendix C. Only a subset of those profiles which is representative of the overall trends and behaviors is shown here. We focus solely on the suction side of the wings, both here and in the appendix. This choice is motivated by the higher Reynolds number and more interesting behavior exhibited on the suction side. Information concerning the pressure side of the wings, as well as the suction side, including all turbulence statistics, is accessible in the simulation database (please refer to the data availability statement).

The initial pattern identified in figure 9 (a) and (b) reveals an overall increase in $R_{11}^+ = R_{11}/u_\tau^2$ in the direction of development of the streamlines (i.e., increasing x') and the emergence of a more active outer region. This is observed in both finite-span and infinite-span profiles and exhibits considerable similarity across both types. This phenomenon is attributed to the adverse-pressure-gradient effects, a topic extensively studied in the literature (cf. Spalart & Watmuff 1993; Perry *et al.* 2002; Aubertine & Eaton 2005; Monty *et al.* 2011; Harun *et al.* 2013; Bobke *et al.* 2017; Bross *et al.* 2019; Pozuelo *et al.* 2022; Devenport & Lowe 2022). Despite its significance, this phenomenon is not the primary focus of this study. Instead, our attention is devoted exclusively to exploring the differences between the finite- and infinite-span boundary layers.

Figure 9 (b) demonstrates a reduction in the near-wall peak of R_{11}^+ , which appears to magnify downstream. This discrepancy mainly arises due to the milder adverse pressure gradient experienced by the boundary layer closer to the tip. This is a consequence of the lower effective angle of attack in that region.

Another trend evident in figure 9 (b) is the increased Reynolds stress level in the outer region of the boundary layer, particularly near its edge. This effect becomes more pronounced in spanwise locations closer to the tip (compare figures 9 (a) and (b)), and it displays a growing spanwise influence as one moves downstream (compare figures 9 (c) and (d)). This phenomenon can be attributed to the increased wall-normal velocity and its wall-normal gradient closer to the wing's tip. This is illustrated in figure 10 (a) for two streamwise locations. The increased wall-normal velocity results in increased boundary layer growth (enhanced $\partial \langle u_1 \rangle_\tau / \partial x_\tau$ due to the continuity equation) and an increased boundary layer thickness, manifesting as a non-zero Reynolds stress at greater distances from the wall. It is worth noting that the spanwise variation in wall-normal velocity diminishes as one moves

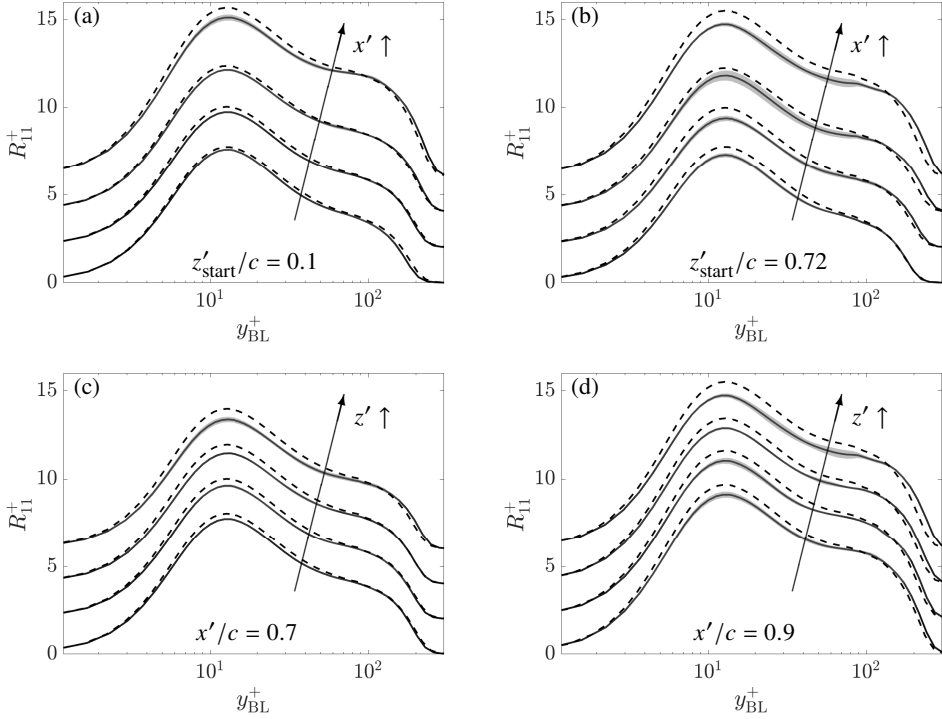


Figure 9: Variation of the inner-scaled Reynolds stress R_{11}^+ with (a,b) streamwise distance from the leading edge, and (c,d) spanwise distance from the root. Panels (a) and (b) correspond to the evolution along streamlines released at $(x'_{\text{start}}, z'_{\text{start}})/c = (0.12, 0.1)$ and $(x'_{\text{start}}, z'_{\text{start}})/c = (0.12, 0.72)$, respectively. Panels (c) and (d) show the locations corresponding to the intersection of four streamlines released at $x'_{\text{start}}/c = 0.12$ at spanwise locations $z'_{\text{start}}/c = 0.1, 0.31, 0.51, 0.72$, with planes at (c) $x'/c = 0.6$ and (d) $x'/c = 0.9$. Profiles are shifted vertically by 2 units with increasing x' or z' for visual clarity. The profiles are from RWT-5 (solid lines) and P-2 (dashed lines), and are a subset of those plotted in figure 13. All streamlines are released in the near-wall (approximately collateral) region. See text and appendix C for more details. Shaded regions correspond to 80% confidence intervals of the inner-scaled Reynolds stress profiles (due to finite time averaging), computed from the non-overlapping batch method (cf. Conway 1963). P-2 has extremely narrow confidence intervals which are not plotted.

downstream. Such observations suggest that the widening spanwise influence of this effect originates from the upstream state of the boundary layer, its flow development towards the root, and propagation of non-zero fluctuations in the spanwise direction (due to mixing and transport).

At these low Reynolds numbers, the development length available for the boundary layers, proportional to c/δ_{99} , is quite limited. This results in a transient response from the boundary layers to the change in their thickness, primarily characterized as a shift in the location of the outer structures away from the wall, which propagates throughout the boundary layer thickness as it develops. This hypothesis is examined in figure 10 (b), where the profiles from figure 9 (b) are shown in outer units. These profiles are contrasted in the figure with their infinite-span counterparts at matched $(Re_\tau, \beta_{x_\tau})$ and matched δ_{99} . A shift in the location of the outer structures away from the wall would manifest itself as a coincident Reynolds stress profile near the boundary layer edge, which is indeed the observed behavior in figure 10 (b). The wall-normal extent of agreement around the boundary layer edge decreases downstream.

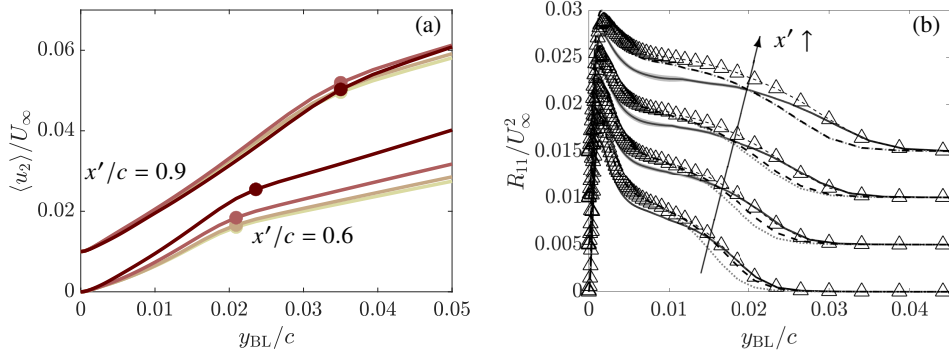


Figure 10: The variation of wall-normal velocity along the span at two streamwise planes (a) and the variation of the outer-scaled R_{11} in the streamwise direction (b). All solid lines correspond to RWT-5. Darker colors in panel (a) denote locations closer to the tip at the intersection of the same streamlines used in figure 9. Profiles shown in panel (b) are the same plotted in figure 9 (b), with dotted lines corresponding to matched x' locations from P-2, and dashed lines corresponding to matched Re_{τ} and $\beta_{x_{\tau}}$ (simple dashed lines) and matched boundary layer thickness δ_{99} (dashed lines with triangles), both from P-2. Profiles are shifted vertically by 0.01 units in panel (a) and 5×10^{-3} units in panel (b) for visual clarity. Shaded regions in panel (b) correspond to 80% confidence intervals in the outer-scaled Reynolds stress profiles (due to finite time averaging), computed from the non-overlapping batch method. Panel (a) has narrow confidence intervals which are not plotted.

This phenomenon may be attributed to the development of the boundary layers and their gradual response to the changes induced by the increased boundary layer thickness. Further implications of this behavior are discussed later.

The spanwise variation of R_{11}^+ is illustrated in figure 9 (c) and (d). A trend of diminishing magnitude in the near-wall peak of the Reynolds stress is evident, particularly when approaching the tip. This phenomenon can be attributed to a few underlying mechanisms.

First, the effective angle of attack, which varies in the spanwise direction, diminishes closer to the tip. As a result, milder adverse pressure gradients occur near the tip (characterized by lower $\beta_{x_{\tau}}$ values). This leads to a lower increase in the inner-scaled Reynolds stress profile and the turbulent kinetic energy due to adverse pressure gradients (in their development in the streamwise direction). Consequently, the overall inner-scaled Reynolds stress levels decrease, resulting in a diminished near-wall peak. In RWT-10 (see figure 14), there is a larger variation in α_{eff} and $\beta_{x_{\tau}}$ across the span compared to RWT-5, which can partially explain the steeper decline of the near-wall peak in RWT-10.

Closer to the tip, the increased deflection angle near the wall results in laminar flow entrainment into the turbulent boundary layers at their outmost spanwise extent. This entrainment is more pronounced in the collateral region $y_{BL}^+ \leq 30$ with the highest deflection angles. Consequently, diminished near-wall turbulence activity can be expected close to the spanwise edge of the turbulent boundary layers. Such reductions in turbulence can influence the near-wall peak of R_{11}^+ outside areas directly subjected to flow entrainment. This could be another reason for the observed decline of the near-wall peak for locations plotted in figure 9. Further investigations are necessary to evaluate the significance of this mechanism in comparison to others.

The other mechanism that contributes to attenuation of the near-wall peak of R_{11}^+ is linked to the discussed increase in growth rate of the boundary layers near the tip. This, on the one hand, reduces the production term near the wall through decreased velocity gradients in the

wall-normal direction, and on the other, leads to additional transport away from the wall. Both of these mechanisms contribute towards reducing the peak in R_{11}^+ profiles.

Another element to consider is the spanwise pressure gradient present within the boundary layers, quantified by β_{z_τ} in tables 3, 4, and 5. To take advantage of the findings of Lozano-Durán *et al.* (2020), an equivalent expression for their parameter Π can be established by considering the relation $\partial\langle p\rangle/\partial x = \tau_w/\delta$ in fully-developed channel flows (where δ is the channel half-height). This leads to a definition of Π in turbulent boundary layers as:

$$\Pi \approx \frac{\delta_{99}}{\tau_w} \frac{\partial P_e}{\partial z_\tau} = \frac{\delta_{99}}{\delta^*} \beta_{z_\tau}.$$

This parameter was found to be always below $0.015Re_\tau$ at all locations reported here and in figures 12, 13, and 14. This is well below the range of the approximate value of $\Pi > 0.03Re_\tau$ suggested by Lozano-Durán *et al.* (2020) as the regime in which the effect of spanwise pressure gradients become significant. As a result, it is unlikely for this mechanism to have a significant impact on the attenuation of turbulence and the near-wall peak of the Reynolds stress profile. It should be noted that the recommended criterion was derived for higher Re_τ , in the absence of adverse pressure gradients, and for an initially fully-developed channel flow. Whether a violation of these conditions leads to significant departures from the proposed criterion is not entirely clear and merits further investigation.

It is important to acknowledge certain observed departures in figures 12, 13, and 14 from the trends described above. Firstly, RWT-0 exhibits a profile almost identical to P-0 near the root at $x'/c = 0.6$ (figure 12 (a)), yet later evolves to display lower levels of fluctuations for $y_{BL}^+ \geq 30$ at downstream locations as early as $x'/c = 0.7$, despite having the same boundary layer thickness. While this is most likely an artifact caused by differences in the trip or different response of the boundary layers to the trip (e.g., a history effect), further investigations are needed to ascertain whether this might be a consequence of additional unidentified mechanisms. Another noticeable departure is found in the case of RWT-10, particularly at $x'/c = 0.8$ and 0.9 (figures 14 (k), (l), (o) and (p)), which do not display a decrease in the near-wall peak. Possible explanations for this behavior could include the larger variation of β_{x_τ} at those locations, the reduced deflection angle at $x'/c = 0.8$ and 0.9 (see figure 5 (c)), and the stronger three-dimensional effects in RWT-10.

Before concluding this section, we should emphasize that the reference profiles chosen for the comparisons in this section were specifically selected to eliminate as many causes of difference between the finite- and infinite-span profiles as possible. This ensures that the observed differences primarily arise from a few key mechanisms. However, this selection also results in smaller differences between the compared profiles, which may not be fully representative of the real discrepancy. This point is partially illustrated in figure 10 (b), which shows a larger difference in R_{11} profiles when only the streamwise locations are matched. It is worth noting that, at the spanwise location selected for this figure, RWT-5 exhibits a reduced effective angle of attack of approximately 1° . Given that a decreased effective angle of attack leads to thinner boundary layers and a higher outer-scaled near-wall peak in R_{11} , the actual disparity between the finite- and infinite-span wings is likely greater than what is depicted in the figure.

5. Summary and conclusions

High-fidelity simulations of finite-span wings with a symmetric NACA0012 profile and a rounded wing tip geometry were performed at a chord-based Reynolds number of 200 000 in free-flight conditions. Three angles of attack (0° , 5° , and 10°) were considered and supplemented with infinite-span (periodic) wings at corresponding geometric and effective

angles of attack. Tripping was used to ensure turbulent boundary layers on both the suction and pressure sides. The resulting database can be used for a number of academic and engineering applications, including careful studies of the boundary layers and the wake, the wing-tip vortex and its formation, development and interaction with the surrounding flow, or improving the turbulence models such as the Reynolds-averaged Navier–Stokes (RANS) models or wall models used in LES. The main focus here was on the effect of wing-tip vortices and their induced three-dimensionality on the turbulent boundary layers. Other aspects of the flow will be studied in future works.

The general flow field of the lift-generating wings (RWT-5 and RWT-10) was characterized by the presence of a main wing-tip vortex as well as additional secondary vortices formed on the suction side of the wings. These vortices were stronger and formed earlier for higher angles of attack. A spanwise pressure gradient was present in all finite-span cases (a well-known inviscid effect), including RWT-0 which does not generate lift. As a result of this pressure gradient the boundary layers were deflected towards the root on the suction side and towards the tip on the pressure side. The deflection angle was different across the span and chord of the wing, but also in the wall-normal direction due to the faster response of the low momentum fluid near the wall (see Devenport & Lowe 2022, and references therein).

Despite the non-canonical nature of these boundary layers, they could be simplified by first accounting for the effective angle of attack and its impact on the pressure gradient imposed on the boundary layers, followed by a (tensor) rotation into a coordinate system aligned with the direction of wall shear. This could further simplify the structure of the Reynolds stress tensor and make it similar to a 2D boundary layer, where $R_{13} \approx R_{23} \approx 0$. Two additional effects were observed and discussed. Firstly, the variable deflection angle across the boundary layer thickness means that the fluid particles across a wall-normal line have converged from different spanwise locations, and due to the variable pressure gradient across the span have different histories. Secondly, the variable wall-normal velocity along the span, with higher values closer to the tip, leads to a higher growth rate for the boundary layer farther from the root. Each of these mechanisms has additional consequences. The normal streamwise Reynolds stress R_{11} (as well as the other components) of the finite-span boundary layers were compared with their corresponding profiles from infinite-span wings, the observed differences were explained, and the mechanisms at play were discussed. Some of these differences could not be fully explained by the simplified representation here and thus need further investigations.

Different terms in the transport equation of the turbulent kinetic energy and Reynolds stresses (i.e., the budget terms; see Pope 2000) were computed (and are available in the simulation database; see the data availability statement), but were not shown or discussed here. This was because no additional insight was gained from those terms. For example, while a decrease in the production of R_{11} was observed near the wall, this was as much a consequence of the decreased near-wall peak of R_{11} as it was a cause. Similarly, the increase in the production term near the boundary layer edge and a corresponding increase in the dissipation term could be attributed to the increased R_{11} in that region and the required balance between different terms. This highlights the need for predictive models in wall turbulence.

It is important to emphasize that the assumptions leading to section 4.3, and the subsequent conclusions, are not valid close to the wing-tip vortex or the trailing edge of the wing. For instance, for spanwise locations slightly closer to the tip than those discussed here, while still inside the turbulent region of the boundary layer, the near-wall streamlines have entered from the laminar flow region near the vortex. At the trailing edge, the boundary layer on the suction side with a spanwise velocity towards the root (i.e., $\langle u_3 \rangle < 0$) approaches the boundary layer on the pressure side with its spanwise velocity towards the tip ($\langle u_3 \rangle > 0$).

The two boundary layers also have opposite wall-normal and different streamwise velocities. These complex trailing edge effects were not discussed here.

Throughout this work we relied on quantities such as the Clauser pressure-gradient parameter, with little modification in their formulation or discussion about their application in complex or three-dimensional boundary layers. Here, the three-dimensional effects were somewhat weak and we mostly relied on qualitative comparisons; therefore, the current definitions were deemed sufficient. Going forward, careful studies on the role and optimal definition of such parameters in 3D boundary layers, and potentially developing new ones, are absolutely essential.

Many of the attributes of 3D turbulent boundary layers (summarized in Devenport & Lowe 2022) were not observed here. This includes effects such as depressed wake of the mean velocity profile (cf. Spalart *et al.* 2008), reduction in the Townsend’s structure parameter (cf. Littell & Eaton 1994), or a significant change in the pressure-strain term (cf. Lozano-Durán *et al.* 2020). This is most likely due to the relatively weak variation of the deflection angle in the wall-normal direction, and the gradual variation of this and other similar parameters along the streamlines, both of which allow the boundary layers to recover (or approach) their two-dimensional state. In terms of modeling, the weak three-dimensionality of these boundary layers makes it easier to adapt the current turbulence models to account for these effects.

The wings of this study had a relatively low aspect ratio of 1.5. This was a deliberate choice, motivated by the scope of this study, the stronger three-dimensional effects near the tip, and as a measure to save cost. For a fixed Reynolds number, a wing with a higher aspect ratio will experience a higher effective angle of attack and a stronger vortex. It will also have a slightly different spanwise variation in its effective angle of attack due to the change in the spanwise distance to the mirror vortex. A potentially more significant impact of the low aspect ratio is the (global) blocking effect of the symmetry plane on the spanwise velocity, which could lead to higher variations in the deflection angle along the span or a slightly different location of the wing-tip vortex. While it is important to keep these in mind when generalizing the findings of this study, such effects are most likely secondary to the mechanisms discussed here, and are therefore not expected to change any of the conclusions.

Only straight, rectangular geometries with rounded wing tips were considered for finite-span wings. This was another deliberate choice to minimize the potential differences between the finite- and infinite-span wings and help facilitate our analysis. For that reason, several factors present in realistic wing designs were excluded. These include more realistic airfoil profiles and tip geometries, drag reduction devices, wing sweep and twist, or variable chord and thickness. In addition, the spanwise pressure distribution on the wings was different from the (nearly) elliptic distribution encountered in realistic wings. Compressible effects were also not considered here. It is important to be aware of these differences when generalizing the findings of this work.

It is also important to acknowledge that the present simulations were performed at relatively low Reynolds numbers, which could have an impact on some of the conclusions. In general, increasing the Reynolds number leads to thinner boundary layers on the wing, i.e., smaller values for δ_{99} and δ^* , and higher values of wall-shear stress. This, in principle, leads to a decrease in the streamwise and spanwise Clauser pressure-gradient parameters and a subsequent reduction in the effect of both the streamwise and spanwise pressure gradients. It would also reduce the variation of the deflection angle γ_{stream} in the wall-normal direction, which was the source of variation in flow history. Furthermore, the spanwise variation of boundary layer thickness would occur over longer distances in terms of δ_{99} . In other words, most of the non-equilibrium and three-dimensional effects discussed here tend to diminish with increased Reynolds number. Of course, these predictions and extrapolations need to be

confirmed directly by additional experimental and numerical studies of these flows at a wider range of Reynolds numbers and pressure gradients.

From a computational perspective, one of the main challenges in studying turbulent boundary layers with no homogeneous direction (such as the ones studied here) is the excessively long integration times required for accurate statistics in high-fidelity simulations. Here, we relied on a filtering method along the streamlines with a variable filter width in the spanwise direction. This was an *ad hoc* choice made based on our prior experience and the observed or expected physics of the flow; i.e., relation between variations in γ_{stream} and the rate of change of solution statistics. Given the importance of 3D boundary layers and their prevalence in engineering applications, developing more general, more accurate, and more robust methods for improving statistical convergence is absolutely necessary. Additionally, designing an optimal computational grid for complex flows and geometries is an extremely difficult and time consuming task which, despite the recent advancements in error estimation and grid specification, requires further developments. Addressing such challenges is essential for future studies of more realistic three-dimensional boundary layers.

Acknowledgements. We acknowledge PRACE for awarding us access to HAWK at GCS@HLRS, Germany. We also acknowledge the EuroHPC Joint Undertaking for awarding this project access to the EuroHPC supercomputer LUMI, hosted by CSC (Finland) and the LUMI consortium through EuroHPC Regular Access and EuroHPC Extreme Scale Access calls. Additional computations, data handling, and post-processing were enabled by resources provided by the National Academic Infrastructure for Supercomputing in Sweden (NAISS) and the Swedish National Infrastructure for Computing (SNIC) at PDC partially funded by the Swedish Research Council through grant agreements no. 2022-06725 and no. 2018-05973.

Funding. This work was supported by the European Research Council (ERC), the Swedish Research Council (VR), and the Knut and Alice Wallenberg Foundation. RV acknowledges financial support from the ERC Grant No. “2021-CoG-101043998, DEEPCONTROL”. Views and opinions expressed are however those of the authors only and do not necessarily reflect those of the European Union or the European Research Council. Neither the European Union nor the granting authority can be held responsible for them.

Declaration of interests. The authors report no conflict of interest.

Data availability statement. The data that support the findings of this study will be made openly available, upon publication of the manuscript, in the following repository: <https://www.vinuesalab.com/databases/>

Author ORCID. S. Toosi, <https://orcid.org/0000-0001-6733-9744>; A. Peplinski, <https://orcid.org/0000-0002-7448-3290>; P. Schlatter, <https://orcid.org/0000-0001-9627-5903>; R. Vinuesa, <https://orcid.org/0000-0001-6570-5499>

Appendix A. Post-processing, filtering, and averaging

A total of 44 fields are collected during runtime to compute the statistics. These include the temporal average of u_i and p (velocity and pressure fields), $u_i u_j$ (six independent terms), $u_i u_j u_k$ (ten independent terms), pu_i , $p \partial u_i / \partial x_j$, $\partial u_i / \partial x_k \cdot \partial u_j / \partial x_k$, and a few other fields (see Vinuesa *et al.* 2017a). These fields are then used to compute the additional fields (such as the first and second derivatives of $\langle u_i \rangle$ and $\langle u_i u_j \rangle$) required for computing the Reynolds stress budgets and other statistics, resulting in a total of 99 additional fields. Everything so far is done on the original grids of table 1 using Nek5000’s numerical operators. The remaining operations are point-wise and can be performed on a smaller grid. Therefore, these 143 fields are interpolated from the original unstructured grids used for simulations onto a structured post-processing grid (with an order of magnitude fewer grid points and covering only the near-wing region) which has a nearly-uniform streamwise and spanwise spacing of $(\Delta x, \Delta z)/c = (12.5, 7.8) \times 10^{-4}$ (selected based on an approximate friction length

of $\delta_v = 10^{-4}$) over the majority of the turbulent boundary layer regions of the wing. This is done to facilitate the next post-processing steps, including the spatial filtering.

The spatial filtering is employed for two main reasons: (i) to reduce some of the artifacts present in the derivatives of the solution inherent to spectral-element methods, which are small in our simulations but could still impact some of the more sensitive budget terms, and (ii) to act as a form of spatial averaging and reduce the required integration time of the finite-span configurations.

In the finite-span wings, the employed spatial filter has a two-dimensional Gaussian kernel with its principal axes aligned with the streamlines and the spanwise direction. In the periodic wings, the filter has a one-dimensional kernel along the streamlines. The streamwise filter width is small, and comparable to the size of the spectral elements in that direction, i.e., $2\sigma_x/c \approx 12.5 \times 10^{-3}$ (equivalent to around $125\delta_v$) for element sizes of around $7.4 \times 10^{-3}c$. This is to target the potential artifacts present in element boundaries (cf. Massaro *et al.* 2023) and is common between the finite- and infinite-span wings. In the finite-span wings, the Gaussian filter has a variable spanwise filter width which is a function of both x' and z' , and simultaneously targets the artifacts at the element boundaries (elements are around $5 \times 10^{-3}c$ in size in the spanwise direction) and acts as a form of spanwise averaging to reduce the required integration time. In the periodic wings, the fields are already averaged in the spanwise direction and no spanwise filtering is required. Note that no filtering is used in the wall-normal direction in either of the periodic or finite-span configurations. It is worth mentioning that at first we tried to remove the artifacts at the element boundaries by using a median filter, but it became obvious that it introduced additional artifacts in the budget terms and was therefore quickly abandoned.

The spanwise filter width of the finite-span wings is defined based on the variation in the streamline deflection angle γ_{stream} at the edge of the boundary layer (see figure 8). The main reason for using the value of γ_{stream} at the edge of the boundary layer (as opposed to the arguably more important value at the wall, or somewhere inside the boundary layer) is for its relatively low uncertainties due to time-averaging errors. Additionally, the values of γ_{stream} at the wall and inside the boundary layer are directly related to the value at the edge. These two reasons made γ_{stream} at the boundary layer edge a suitable quantity for our purpose. The spanwise filter width is defined by the following procedure: (i) identifying the variation of γ_{stream} at the boundary layer edge across z' from the root $z'/c = 0$ up to a location where the flow is identified as a turbulent boundary layer (excluding the region strongly affected by the wing-tip vortex or laminar flow entrance), (ii) dividing the variation into 10 equal intervals, finding the location of the dividing boundaries, and computing the size of each interval, (iii) using a linear fit to the identified interval sizes such that it matches the value exactly at the root and the closest location to the tip (to ensure a smooth variation of the filter width along the span, and to avoid overshoots and undershoots typical of higher-order polynomial fits), (iv) defining the filter width by requiring that 80% of the kernel weight lies within the (interpolated) interval size at that location (i.e., divide the interpolated interval size by $2Z_{0.9} \approx 2.56$, where $Z_{0.9}$ is the location of 90th percentile in a normal cumulative distribution function). With this method the spanwise filter width is different for different flows, at different x' and z' locations, and on different sides of the wing, but on the suction side has typical values of $2\sigma_z/c \approx 12 \times 10^{-2}$ at the root and $2\sigma_z/c \approx 3 \times 10^{-2}$ near the tip. One could use the approximate relation $\delta_v/c \gtrsim 10^{-4}$ to convert these values into wall units.

The implementation of the filter was verified by comparing the statistics of P-2 computed using the classical spanwise averaging (over the entire span) to those computed by spanwise filtering, and making sure that the filtered statistics converge to the spanwise averaged ones for wider filter widths.

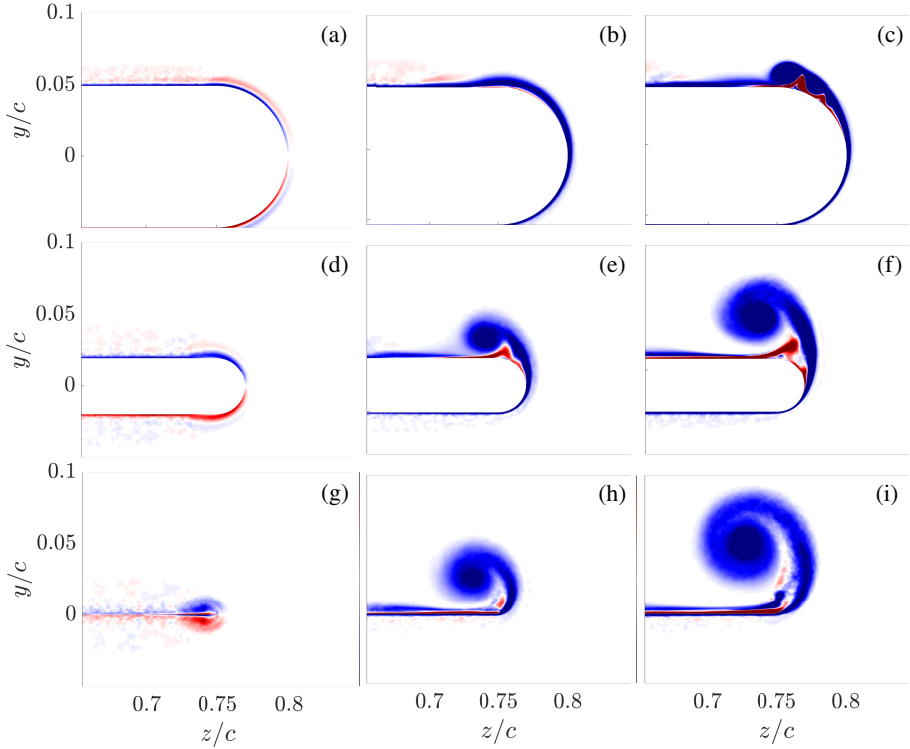


Figure 11: Pseudocolor plots of streamwise vorticity in the vicinity of the wing tip for (left column) RWT-0, (middle column) RWT-5, and (right column) RWT-10. Different rows correspond to different locations along the chord at $x'/c = 0.55, 0.85,$ and 1.0 , from top to bottom. Colormap is from $\langle \omega_1 \rangle c / U_\infty = -50$ (dark blue) to 50 (dark red).

Appendix B. The wing-tip region

Figure 11 shows the mean streamwise vorticity of the flow $\langle \omega_1 \rangle = \langle \partial u_3 / \partial y \rangle - \langle \partial u_2 / \partial z \rangle$ at a few streamwise locations near the tip of RWT-0, RWT-5, and RWT-10 wings. Here, the wing-tip vortex is characterized by a large negative streamwise vorticity region, which is nearly circular in shape (i.e., approximately homogeneous in the azimuthal direction around the core) after separation from the wing surface (e.g., at the trailing edge, see figures 11 (h) and (i)). In addition to the primary wing-tip vortex, one smaller vortex with an opposite direction of rotation can be observed in RWT-5, and two additional vortices (one with opposite rotation, one with the same direction of rotation) in RWT-10. These are the secondary and tertiary vortices formed during the formation of the primary (i.e., the wing-tip) vortex (best visible in figure 11 (f)), and the same vortices identified in figures 5 (b) and (c) as additional streamline spirals. The three-dimensionality of RWT-0 and its curved streamlines manifest as regions of non-negative streamwise vorticity in figures 11 (a), (d) and (g). Interestingly, the streamwise vorticity of RWT-0 near the wall (mostly related to the wall-normal variations in the spanwise velocity; i.e., $\partial \langle u_3 \rangle / \partial y$) could even exceed that of RWT-5; for instance, when comparing figures 11 (d) and (e). It is also worth mentioning that there is a set of counter-rotating vortices formed at the trailing edge of RWT-0, figure 11 (g), as mentioned by Giuni & Green (2013).

The pressure gradients caused by the pressure difference between the suction and pressure sides of the lift-generating wings lead to a strong flow acceleration from the pressure side towards the suction side. While this flow remains attached to the surface for lower pressure

gradients, for instance figure 11 (b), it eventually separates from the wing surface resulting in the formation of the primary (i.e., wing-tip) vortex, for instance in figure 11 (c). This in turn leads to the formation of additional (secondary, tertiary, ...) vortices that could either grow larger, as in figures 11 (c) and (f), or combine with the primary vortex and dissipate, as in figures 11 (e) and (h).

An important distinction should be made between the vortex formation described here and that of an inviscid flow. In particular, in the absence of viscosity and no-slip boundary conditions at the wall the wing-tip vortex only separates farther downstream near the tip of the trailing-edge where the radius of curvature approaches zero (cf. Rizzi & Eriksson 1984). The change in the location of the vortex leads to variations in the induced downwash on the wing. As was observed in figure 7 such variations are rather small away from the vortex core and become significant only closer to the wing tip. Additionally, the formation of secondary and tertiary vortices are not observed in inviscid flows.

Appendix C. More details on the comparison of boundary layer quantities for finite- and infinite-span wings

The boundary layer histories are approximately matched by comparing the finite-span wing with a periodic one at a similar effective angle of attack, and thus pressure-gradient history. Here, the effective angles of attack are only matched at the root, and therefore larger differences are expected closer to the tip of the wings. The remaining differences in tripping, or the response of the boundary layer to the trip, can also add to these differences. These are, however, less significant on the suction side of the wings considered here.

In order to find an equivalent profile in terms of the local Re_τ and β_{x_τ} , a location on the periodic wing is found that is closest to the Re_τ and β_{x_τ} values of the selected location on the finite-span wing based on a distance on the $(Re_\tau, \beta_{x_\tau})$ plane defined as

$$d_{(Re_\tau, \beta_{x_\tau})} = \sqrt{\left(\frac{Re_{\tau, \text{RWT}} - Re_{\tau, \text{P}}}{Re_{\tau, 0}}\right)^2 + \left(\frac{\beta_{x_\tau, \text{RWT}} - \beta_{x_\tau, \text{P}}}{\beta_{x_\tau, 0}}\right)^2},$$

where $Re_{\tau, \text{RWT}}$ and $\beta_{x_\tau, \text{RWT}}$ are the values on the finite-span wing for the selected location, $Re_{\tau, \text{P}}$ and $\beta_{x_\tau, \text{P}}$ are the values for the periodic wing, and $Re_{\tau, 0}$ and $\beta_{x_\tau, 0}$ are user-defined values that weight the two quantities (which have significantly different values) when defining the distance. Here we have chosen $Re_{\tau, 0} = 25$ and $\beta_{x_\tau, 0} = 0.25$, meaning that we expect to see differences between two profiles for a variation in Re_τ that is comparable to 25 (in terms of order of magnitude) and a variation in β_{x_τ} comparable to 0.25. We effectively assume that these levels of variation in the two variables lead to comparable levels of overall departure in the studied profiles.

Figures 12, 13, and 14 show the R_{11} , R_{22} , R_{33} , and R_{12} components of the Reynolds stress $R_{ij} = \langle u'_i u'_j \rangle_\tau$ at different chord-wise and spanwise locations on the suction side of RWT-0, RWT-5, and RWT-10, compared with their corresponding profiles from P-0, P-2, and P-5, at matching Re_τ , β_{x_τ} , and α_{eff} . Four streamlines are released at $x'/c = 0.12$ (i.e., immediately downstream of the trip) at four different spanwise (z') locations: $z'/c = 0.1$, 0.31, 0.51, and 0.72. We then compute the intersection of these streamlines with planes located at the chord-wise locations $x'/c = 0.6, 0.7, 0.8,$ and 0.9 . These are the locations used for plotting the profiles, where we note that the z' locations depend on the flow field and are different at different x' locations and for different angles of attack. The minimum and maximum spanwise locations are selected to avoid the effect of the symmetry plane at the root (although limited to a much smaller spanwise region) and be fully inside the turbulent

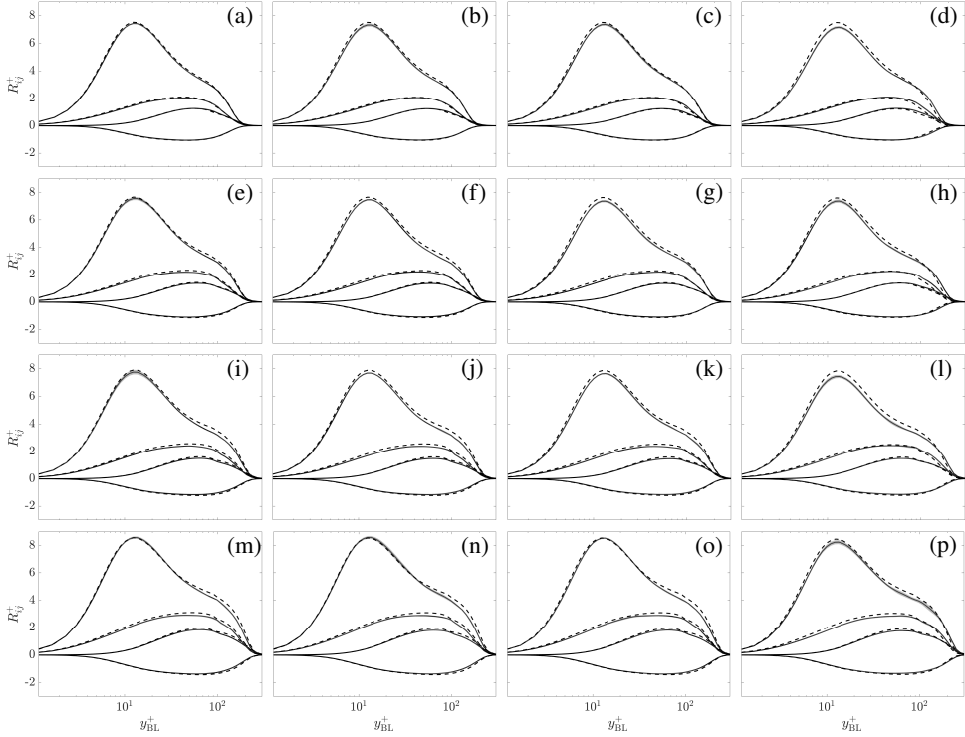


Figure 12: Variation of the Reynolds stresses R_{11} , R_{33} , R_{22} , and R_{12} with distance from the wall in RWT-0 (solid lines) compared to P-0 (dashed lines) at matched $(Re_\tau, \beta_{x_\tau})$ values. Rows from top to bottom correspond to different streamwise locations of $x'/c = 0.6, 0.7, 0.8,$ and 0.9 , respectively. Columns from left to right correspond to spanwise locations of the streamlines near the wall (in the collateral region) released from $x'_{\text{start}}/c = 0.12$ (immediately downstream of the trip) at $z'_{\text{start}}/c = 0.1, 0.31, 0.51,$ and 0.72 , respectively. At each location, the Reynolds stress components are expressed in the local (x_τ, y_τ, z_τ) coordinate system aligned with the direction of wall-shear stress at that specific location. Shaded regions correspond to 80% confidence intervals of the inner-scaled Reynolds stress profiles (due to finite time averaging), computed from the non-overlapping batch method.

region of the flow (tripping only applied to $z'/c < 0.75$; see figure 4). The downstream spanwise locations are selected based on the near-wall streamlines in the collateral region.

Tables 3, 4, and 5 summarize the local friction Reynolds number Re_τ and the Clauser pressure-gradient parameters β_{x_τ} (streamwise) and β_{z_τ} (spanwise) for all the profiles plotted in figures 12, 13, and 14.

REFERENCES

- ATZORI, M., TORRES, P., VIDAL, A., LE CLAINCHE, S., HOYAS, S. & VINUESA, R. 2023 High-resolution simulations of a turbulent boundary layer impacting two obstacles in tandem. *Phys. Rev. Fluids* **8**, 063801.
- AUBERTINE, C. & EATON, J. 2005 Turbulence development in a non-equilibrium turbulent boundary layer with mild adverse pressure gradient. *J. Fluid Mech.* **532**, 345–364.
- BOBKE, A., VINUESA, R., ÖRLÜ, R. & SCHLATTER, P. 2017 History effects and near equilibrium in adverse-pressure-gradient turbulent boundary layers. *J. Fluid Mech.* **820**, 667–692.
- BRADSHAW, P. & PONTIKOS, N. 1985 Measurements in the turbulent boundary layer on an ‘infinite’ swept wing. *J. Fluid Mech.* **159**, 105–130.

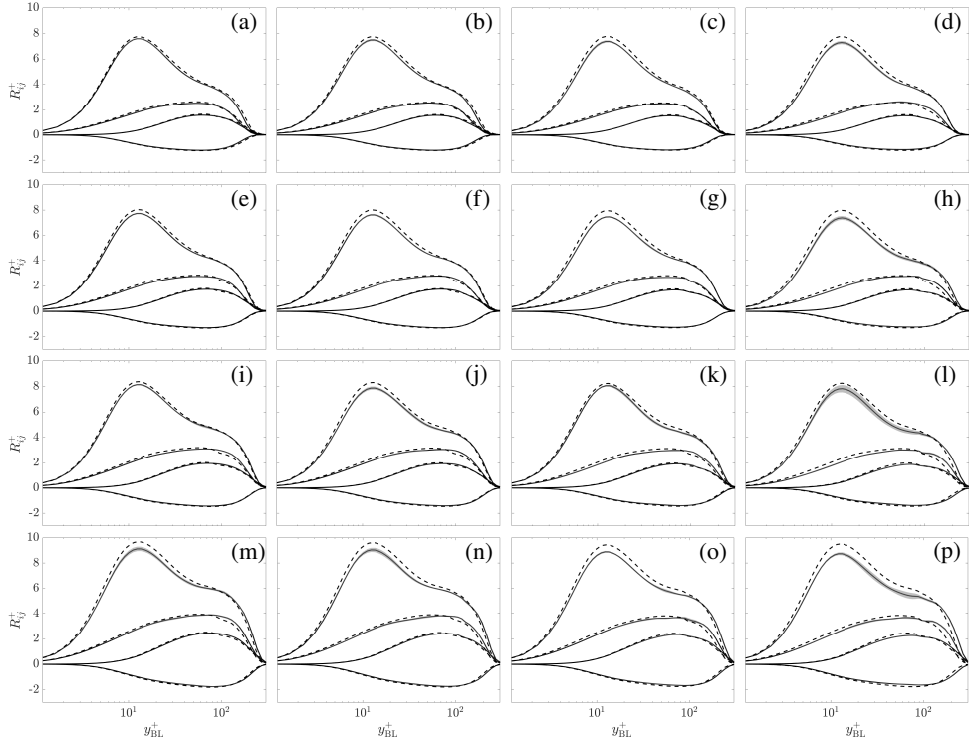


Figure 13: Variation of the Reynolds stresses with wall distance at several streamwise and spanwise locations on the suction side of RWT-5 (solid lines) compared to P-2 (dashed lines) at matching $(Re_\tau, \beta_{x_\tau})$ values. Shaded regions correspond to 80% confidence intervals of the inner-scaled Reynolds stress profiles due to finite time averaging. See the caption of figure 12 for more details.

$\frac{\text{RWT-0}}{\text{P-0}}$	z_1	z_2	z_3	z_4
$x' = 0.6$	$(177, 0.34, 0.01)$ $(176, 0.34)$	$(176, 0.33, 0.03)$ $(174, 0.34)$	$(178, 0.33, 0.06)$ $(173, 0.34)$	$(179, 0.31, 0.14)$ $(170, 0.33)$
$x' = 0.7$	$(201, 0.46, 0.01)$ $(202, 0.46)$	$(201, 0.46, 0.02)$ $(201, 0.46)$	$(201, 0.44, 0.05)$ $(199, 0.44)$	$(211, 0.40, 0.11)$ $(197, 0.43)$
$x' = 0.8$	$(223, 0.73, 0.01)$ $(226, 0.72)$	$(222, 0.71, 0.01)$ $(225, 0.71)$	$(222, 0.70, 0.02)$ $(224, 0.69)$	$(234, 0.65, 0.04)$ $(223, 0.67)$
$x' = 0.9$	$(238, 1.48, 0.00)$ $(244, 1.48)$	$(238, 1.46, 0.00)$ $(244, 1.46)$	$(239, 1.46, -0.03)$ $(244, 1.46)$	$(252, 1.37, -0.15)$ $(243, 1.38)$

Table 3: The set of three values in the numerator are $(Re_\tau, \beta_{x_\tau}, \beta_{z_\tau})$ for RWT-0 at the locations plotted in figure 12. The pair of values in the denominator are $(Re_\tau, \beta_{x_\tau})$ for the P-0 profiles plotted for comparison.

- BROSS, M., FUCHS, T. & KAHLER, C. J. 2019 Interaction of coherent flow structures in adverse pressure gradient turbulent boundary layers. *J. Fluid Mech.* **873**, 287–321.
- CERON-MUNOZ, H., COSIN, R., COIMBRA, R., CORREA, L. & CATALANO, F. 2013 Experimental investigation of wing-tip devices on the reduction of induced drag. *AIAA J. Aircraft* **50** (2), 441–449.
- CHOW, J., ZILLIAC, G. & BRADSHAW, P. 1997a Mean and turbulence measurements in the near field of a wingtip vortex. *AIAA J.* **35** (10), 1561–1567.
- CHOW, J., ZILLIAC, G. & BRADSHAW, P. 1997b Turbulence measurements in the near field of a wingtip vortex. *NASA Technical Memorandum* **110418**.
- CLAUSER, F. 1954 Turbulent boundary layers in adverse pressure gradients. *J. Aero. Sci.* **21** (2), 91–108.

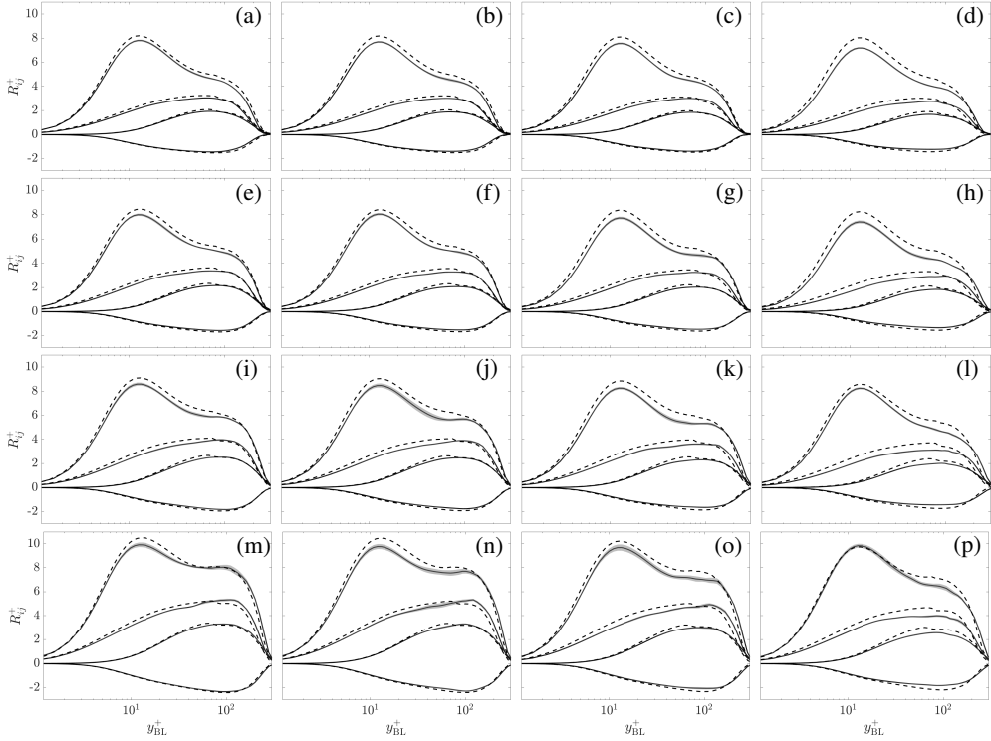


Figure 14: Variation of the Reynolds stresses with wall distance at several streamwise and spanwise locations on the suction side of RWT-10 (solid lines) compared to P-5 (dashed lines) at matching $(Re_\tau, \beta_{x_\tau})$ values. Shaded regions correspond to 80% confidence intervals of the inner-scaled Reynolds stress profiles due to finite time averaging. See the caption of figure 12 for more details.

$\frac{RWT-5}{P-2}$	z_1	z_2	z_3	z_4
$x' = 0.6$	$\frac{(208, 0.74, 0.03)}{(222, 0.70)}$	$\frac{(207, 0.72, 0.07)}{(220, 0.68)}$	$\frac{(208, 0.68, 0.12)}{(215, 0.64)}$	$\frac{(214, 0.68, 0.11)}{(218, 0.67)}$
$x' = 0.7$	$\frac{(233, 0.96, 0.03)}{(240, 0.95)}$	$\frac{(232, 0.94, 0.06)}{(239, 0.92)}$	$\frac{(235, 0.88, 0.09)}{(237, 0.87)}$	$\frac{(243, 0.88, 0.03)}{(238, 0.89)}$
$x' = 0.8$	$\frac{(255, 1.42, 0.03)}{(254, 1.43)}$	$\frac{(254, 1.37, 0.04)}{(253, 1.37)}$	$\frac{(258, 1.31, 0.03)}{(252, 1.32)}$	$\frac{(266, 1.30, -0.12)}{(252, 1.33)}$
$x' = 0.9$	$\frac{(267, 2.65, 0.02)}{(259, 2.67)}$	$\frac{(267, 2.59, 0.01)}{(260, 2.60)}$	$\frac{(273, 2.44, -0.06)}{(260, 2.45)}$	$\frac{(281, 2.51, -0.44)}{(260, 2.51)}$

Table 4: The local friction Reynolds number and Clauser pressure-gradient parameters of RWT-5 (numerator) and P-2 (denominator) for the profiles plotted in figure 13. See the caption of table 3 for more details.

CLAUSER, F. 1956 The turbulent boundary layer. *Adv. Appl. Mech.* **4**, 1–51.

COLEMAN, G., KIM, J. & SPALART, P. 2000 A numerical study of strained three-dimensional wall-bounded turbulence. *J. Fluid Mech.* **416**, 75–116.

CONWAY, R. W. 1963 Some tactical problems in digital simulation. *Manag. Sci.* **10** (1), 47–61.

DEGANI, A., SMITH, F. & WALKER, J. 1993 Theoretical and numerical study of a three-dimensional turbulent boundary layer. *J. Fluid Mech.* **250**, 43–48.

DEVENPORT, W. & LOWE, K. 2022 Equilibrium and non-equilibrium turbulent boundary layers. *Prog. Aero. Sci.* **131**, 100807.

$\frac{\text{RWT-10}}{\text{P-5}}$	z_1	z_2	z_3	z_4
$x' = 0.6$	$\frac{(240, 1.33, 0.05)}{(249, 1.26)}$	$\frac{(239, 1.27, 0.09)}{(248, 1.24)}$	$\frac{(237, 1.16, 0.12)}{(244, 1.13)}$	$\frac{(245, 0.99, 0.05)}{(237, 1.05)}$
$x' = 0.7$	$\frac{(263, 1.72, 0.03)}{(266, 1.70)}$	$\frac{(264, 1.63, 0.04)}{(265, 1.64)}$	$\frac{(265, 1.47, 0.00)}{(261, 1.48)}$	$\frac{(273, 1.21, -0.17)}{(254, 1.33)}$
$x' = 0.8$	$\frac{(283, 2.48, 0.01)}{(278, 2.48)}$	$\frac{(284, 2.40, -0.03)}{(278, 2.41)}$	$\frac{(289, 2.19, -0.19)}{(277, 2.19)}$	$\frac{(294, 1.76, -0.55)}{(272, 1.83)}$
$x' = 0.9$	$\frac{(292, 4.20, -0.04)}{(283, 4.22)}$	$\frac{(292, 4.17, -0.18)}{(282, 4.17)}$	$\frac{(298, 3.85, -0.46)}{(282, 3.87)}$	$\frac{(297, 3.31, -1.19)}{(284, 3.31)}$

Table 5: The local friction Reynolds number and Clauser pressure-gradient parameters of RWT-10 (numerator) and P-5 (denominator) for the profiles plotted in figure 14. See the caption of table 3 for more details.

- DEVENPORT, W., RIFE, M., LIAPIS, S. & FOLLIN, G. 1996 The structure and development of a wing-tip vortex. *J. Fluid Mech.* **312**, 67–106.
- DEVENPORT, W., VOGEL, C. & ZSOLDOS, J. 1999 Flow structure produced by the interaction and merger of a pair of co-rotating wing-tip vortices. *J. Fluid Mech.* **394**, 357–377.
- DEVENPORT, W., ZSOLDOS, J. & VOGEL, C. 1997 The structure and development of a counter-rotating wing-tip vortex pair. *J. Fluid Mech.* **332**, 71–104.
- DEVILLE, M., FISCHER, P. & MUND, E. 2002 *High-Order Methods for Incompressible Fluid Flow*. Cambridge University Press.
- DGHIM, M., MILOUD, K., FERCHICHI, M. & FELLOUAH, H. 2021 Meandering of a wing-tip vortex in a grid-generated turbulent flow. *Phys. Fluids* **33**, 115131.
- ECONOMON, T. D., PALACIOS, F., COPELAND, S. R., LUKACZYK, T. W. & ALONSO, J. J. 2016 SU2: An open-source suite for multiphysics simulation and design. *AIAA J.* **54** (3), 828–846.
- EITEL-AMOR, G., ÖRLÜ, R. & SCHLATTER, P. 2014 Simulation and validation of a spatially evolving turbulent boundary layer up to $Re_\theta = 8300$. *Int. J. Heat Fluid Flow* **47**, 57–69.
- EITEL-AMOR, G., ÖRLÜ, R., SCHLATTER, P. & FLORES, O. 2015 Hairpin vortices in turbulent boundary layers. *Phys. Fluids* **27**, 025108.
- FEDERAL AVIATION ADMINISTRATION 2016 Pilot’s handbook of aeronautical knowledge.
- FISCHER, P., LOTTES, J. & KERKEMEIER, S. 2010 NEK5000: Open source spectral element CFD solver. Available at: <http://nek5000.mcs.anl.gov>.
- FISHMAN, G., WOLFINGER, M. & ROCKWELL, D. 2017 The structure of a trailing vortex from a perturbed wing. *J. Fluid Mech.* **824**, 701–721.
- GARMANN, D. & VISBAL, M. 2015 Interactions of a streamwise-oriented vortex with a finite wing. *J. Fluid Mech.* **767**, 782–810.
- GARMANN, D. & VISBAL, M. 2017 Analysis of tip vortex near-wake evolution for stationary and oscillating wings. *AIAA J.* **55** (8), 2686–2702.
- GIUNI, M. & GREEN, R. 2013 Vortex formation on squared and rounded tip. *Aeros. Sci. Tech.* **29**, 191–199.
- HARUN, Z., MONTY, J., MATHIS, R. & MARUSIC, I. 2013 Pressure gradient effects on the large-scale structure of turbulent boundary layers. *J. Fluid Mech.* **715**, 477–498.
- HOSSEINI, S. M., VINUESA, R., SCHLATTER, P., HANIFI, A. & HENNINGSON, D. 2016 Direct numerical simulation of the flow around a wing section at moderate Reynolds number. *Int. J. Heat Fluid Flow* **61**, 117–128.
- HOUGHTON, E., CARPENTER, P., COLLICOTT, S. & VALENTINE, D. 2013 *Aerodynamics for Engineering Students*. Butterworth-Heinemann.
- JEONG, J. & HUSSAIN, F. 1995 On the identification of a vortex. *J. Fluid Mech.* **285**, 69–94.
- JOHNSTON, J. 1960 On the three-dimensional turbulent boundary layer generated by secondary flow. *J. Basic Engr.* **82** (1), 233–246.
- JOHNSTON, J. & FLACK, K. 1996 Review—advances in three-dimensional turbulent boundary layers with emphasis on the wall-layer regions. *J. Fluids Engr.* **118** (2), 219–232.
- KANNAPALLI, C. & PIOMELLI, U. 2000 Large-eddy simulation of a three-dimensional shear-driven turbulent boundary layer. *J. Fluid Mech.* **423**, 175–203.
- KARNIADAKIS, G. E., ISRAELI, M. & ORSZAG, S. A. 1991 High-order splitting methods for the incompressible Navier–Stokes equations. *J. Comput. Phys.* **97**, 414–443.

- KEVIN, MONTY, J. & HUTCHINS, N. 2019 Turbulent structures in a statistically three-dimensional boundary layer. *J. Fluid Mech.* **859**, 543–565.
- KROO, I. 2001 Drag due to lift: Concepts for prediction and reduction. *Annu. Rev. Fluid Mech.* **33**, 587–617.
- LAPENTA, G. 2003 Variational grid adaptation based on the minimization of local truncation error: time-independent problems. *J. Comput. Phys.* **193**, 159–179.
- LAZPITA, E., MARTINEZ-SANCHEZ, A., CORROCHANO, A., HOYAS, S., LE CLAINCHE, S. & VINUESA, R. 2022 On the generation and destruction mechanisms of arch vortices in urban fluid flows. *Phys. Fluids* **34**, 051702.
- LEE, T. & PEREIRA, J. 2010 Nature of wakelike and jetlike axial tip vortex flows. *AIAA J. Aircraft* **47** (6), 1946–1954.
- LITTELL, H. & EATON, J. 1994 Turbulence characteristics of the boundary layer on a rotating disk. *J. Fluid Mech.* **266**, 175–207.
- LOZANO-DURÁN, A., GIOMETTO, M., PARK, G. I. & MOIN, P. 2020 Non-equilibrium three-dimensional boundary layers at moderate Reynolds numbers. *J. Fluid Mech.* **883**, A20.
- MADAY, Y., PATERA, A. T. & RØNQUIST, E. M. 1987 A well-posed optimal spectral element approximation for the stokes problem. In *ICASE Report No. 87–48*.
- MASSARO, D., PEPLINSKI, A. & SCHLATTER, P. 2023 Interface discontinuities in spectral-element simulations with adaptive mesh refinement. In *Spectral and High Order Methods for Partial Differential Equations ICOSAHOM 2020+1*, pp. 375–386. Cham: Springer International Publishing.
- MAVRIPPLIS, C. 1990 A posteriori error estimators for adaptive spectral element techniques. In *Proc. 8th GAMM-Conf. Num. Meth. Fluid Mech.*, pp. 333–342.
- McKENNA, C., BROSS, M. & ROCKWELL, D. 2017 Structure of a streamwise-oriented vortex incident upon a wing. *J. Fluid Mech.* **816**, 306–330.
- MOIN, P., SHIH, T.-H., DRIVER, D. & MANSOUR, N. 1990 Direct numerical simulation of a three-dimensional turbulent boundary layer. *Phys. Fluids A: Fluid Dyn.* **2** (10), 1846–1853.
- MONTY, J., HARUN, P. & MARUSIC, I. 2011 A parametric study of adverse pressure gradient turbulent boundary layers. *Int. J. Heat Fluid Flow* **32**, 575–585.
- NEGI, P., VINUESA, R., HANIFI, A., SCHLATTER, P. & HENNINGSON, D. 2018 Unsteady aerodynamic effects in small-amplitude pitch oscillations of an airfoil. *Int. J. Heat Fluid Flow* **71**, 378–391.
- OFFERMANS, N. 2019 Aspects of adaptive mesh refinement in the spectral element method. PhD thesis. Royal Institute of Technology.
- OFFERMANS, N., PEPLINSKI, A., MARIN, O. & SCHLATTER, P. 2020 Adaptive mesh refinement for steady flows in Nek5000. *Comps & Fluids* **197**, 104352.
- PARK, M. 2003 Three-dimensional turbulent RANS adjoint-based error correction. *AIAA Paper* p. 3849.
- PATERA, A. 1987 A spectral element method for fluid dynamics: Laminar flow in a channel expansion. *J. Comput. Phys.* **54**, 468–488.
- PEPLINSKI, A., OFFERMANS, N., FISCHER, P. & SCHLATTER, P. 2018 Non-conforming elements in Nek5000: pressure preconditioning and parallel performance. In *Spectral and High Order Methods for Partial Differential Equations ICOSAHOM 2018*, pp. 599–609.
- PERRY, A. & JOUBERT, P. 1965 A three-dimensional turbulent boundary layer. *J. Fluid Mech.* **22** (2), 285–304.
- PERRY, A., MARUSIC, I. & JONES, M. 2002 On the streamwise evolution of turbulent boundary layers in arbitrary pressure gradients. *J. Fluid Mech.* **461**, 61–91.
- PHILLIPS, W., HUNSAKER, D. & JOO, J. 2019 Minimizing induced drag with lift distribution and wingspan. *AIAA J. Aircraft* **56**.
- PIERCE, F., McALLISTER, J. & TENNANT, M. 1983 A review of near-wall similarity models in three-dimensional turbulent boundary layers. *J. Fluids Engr.* **105**, 251–256.
- POPE, S. 2000 *Turbulent Flows*. Cambridge University Press.
- POZUELO, R., LI, Q., SCHLATTER, P. & VINUESA, R. 2022 An adverse-pressure-gradient turbulent boundary layer with nearly constant $\beta = 1.4$ up to $Re_\theta \approx 8700$. *J. Fluid Mech.* **939**, A34.
- RIZZI, A. & ERIKSSON, L.-E. 1984 Computation of flow around wings based on the Euler equations. *J. Fluid Mech.* **148**, 45–71.
- ROCKWELL, D. 1998 Vortex-body interactions. *Annu. Rev. Fluid Mech.* **30**, 199–229.
- ROTTA, J. 1979 A family of turbulence models for three-dimensional boundary layers. In *Turbulent Shear Flows 1*, pp. 267–278. Springer.
- SCHLATTER, P. & BRANDT, L. 2010 DNS of spatially-developing three-dimensional turbulent boundary layers. In *Direct and Large-Eddy Simulation VII. ERCOFTAC series, vol 13*. Springer, Dordrecht.

- SCHLATTER, P., LI, Q., BRETHOUWER, G., JOHANSSON, A. & HENNINGSON, D. 2010 Simulations of spatially evolving turbulent boundary layers up to $Re_\theta = 4300$. *Int. J. Heat Fluid Flow* **31** (3), 251–261.
- SCHLATTER, P., STOLZ, S. & KLEISER, L. 2004 LES of transitional flows using the approximate deconvolution model. *Int. J. Heat Fluid Flow* **25**, 549–558.
- SCHLATTER, P. & ÖRLÜ, R. 2012 Turbulent boundary layers at moderate Reynolds numbers: inflow length and tripping effects. *J. Fluid Mech.* **710**, 5–34.
- SPALART, P. 1986 Numerical study of sink-flow boundary layers. *J. Fluid Mech.* **172**, 307–328.
- SPALART, P. 1989 The structure of a three-dimensional turbulent boundary layer. *J. Fluid Mech.* **205**, 319–340.
- SPALART, P. 1998 Airplane trailing vortices. *Annu. Rev. Fluid Mech.* **30**, 107–138.
- SPALART, P. 2008 On the far wake and induced drag of aircraft. *J. Fluid Mech.* **603**, 413–430.
- SPALART, P., COLEMAN, G. N. & JOHNSTONE, R. 2008 Direct numerical simulation of the Ekman layer: A step in Reynolds number, and cautious support for a log law with a shifted origin. *Phys. Fluids* **20**, 101507.
- SPALART, P. & WATMUFF, J. 1993 Experimental and numerical study of a turbulent boundary layer with pressure gradients. *J. Fluid Mech.* **249**, 337–371.
- SUARDI, C. A., PINELLI, A. & OMIYEGANEH, M. 2020 The effect of the sweep angle to the turbulent flow past an infinite wing. In *Direct and Large-Eddy Simulation XII. ERCOFTAC series, vol 27*. Springer, Cham.
- TANARRO, A., MALLOR, F., OFFERMANS, N., PEPLINSKI, A., VINUESA, R. & SCHLATTER, P. 2020 Enabling adaptive mesh refinement for spectral-element simulations of turbulence around wing sections. *Flow Turb. Comb.* **105**, 415–436.
- TOOSI, S. 2019 Error estimation, grid selection, and convergence verification in large eddy simulation. PhD thesis. University of Maryland.
- TOOSI, S. & LARSSON, J. 2017 Anisotropic grid adaptation in large eddy simulations. *Computers and Fluids* **156**, 146–161.
- TOOSI, S. & LARSSON, J. 2020 Towards systematic grid selection in LES: Identifying the optimal spatial resolution by minimizing the solution sensitivity. *Comp. & Fluids* **201**, 104488.
- VAN DEN BERG, B. 1975 A three-dimensional law of the wall for turbulent shear flows. *J. Fluid Mech.* **70**, 149–160.
- VINUESA, R., BOBKE, A., ÖRLÜ, R. & SCHLATTER, P. 2016 On determining characteristic length scales in pressure-gradient turbulent boundary layers. *Phys. Fluids* **28** (5), 055101.
- VINUESA, R., FICK, L., NEGI, P., MARIN, O., MERZARI, E. & SCHLATTER, P. 2017a Turbulence statistics in a spectral element code: a toolbox for high-fidelity simulations .
- VINUESA, R., HOSSEINI, S. M., HANIFI, A., HENNINGSON, D. & SCHLATTER, P. 2017b Pressure-gradient turbulent boundary layers developing around a wing section. *Flow Turb. Comb.* **99**, 613–641.
- VINUESA, R., NEGI, P., ATZORI, M., HANIFI, A., HENNINGSON, D. & SCHLATTER, P. 2018 Turbulent boundary layers around wing sections up to $Re_c = 1,000,000$. *Int. J. Heat Fluid Flow* **72**, 86–99.
- YUAN, J. & PIOMELLI, U. 2015 Numerical simulation of a spatially developing accelerating boundary layer over roughness. *J. Fluid Mech.* **780**, 192–214.
- ÖLÇMEN, S. & SIMPSON, R. 1995 An experimental study of a three-dimensional pressure-driven turbulent boundary layer. *J. Fluid Mech.* **290**, 225–242.